ADVANCES IN INORGANIC CHEMISTRY, VOL. 36

SOLID-STATE BIOINORGANIC CHEMISTRY: MECHANISMS AND MODELS OF BIOMINERALIZATION

STEPHEN MANN* and CAROLE C. PERRY**

* School of Chemistry, University of Bath, Bath BA2 7AY, England, and
** Chemistry Department, Brunel University, Uxbridge, Middlesex UB8 3PH, England

I. Introduction
II. Biomineralization
  A. Silica
  B. Iron Oxides
  C. Group IIA Carbonates and Sulfates
  D. Composite Biominerals; Limpet Teeth
III. Model Systems
  A. Phospholipid Vesicles
  B. Synthetic Studies
  C. Organized Organic Substrates
  References

I. Introduction

Although the study of biomineralization has received much attention from biologists, geologists, and medical scientists, the structure and function of inorganic solids in biological systems has only recently been perceived as an important aspect of bioinorganic chemistry. We believe that much of the impetus for this initiative arises from the vision and insight of Professor R. J. P. Williams, to whom this article is dedicated. The aim is to present an overview of recent advances in solid-state bioinorganic chemistry. As the number of chemistry research groups currently involved in biomineralization is very few, we hope that this paper will encourage other workers into this new field of bioinorganic chemistry.

A particular focus of this review is studies associated directly or indirectly with Professor Williams. For a more extensive coverage of

the chemical aspects of biomineralization, see Ref. *1*. The studies reported emphasize work carried at Oxford (SM, 1978–1984; CCP, 1981–1987), and subsequent developments at the Universities of Bath and Brunel.

As far as we know, there was a deliberate intention of Professor Williams to become involved in biomineralization. It seems clear that he considered the controlled formation of inorganic solids in biology as a natural extension of the field of bioinorganic chemistry. The opportunity to start the work was made possible through the electron microscopy expertise of Dr. A. J. Skarnulis in the Chemical Crystallography Laboratory, Oxford, and the first investigations used both NMR spectroscopy and electron microscopy to study the control of precipitation in unilamellar phosphatidylcholine vesicles (*2*). The experiments involved the binding of Co(II) to the headgroups of the inner membrane surface and could be readily followed by shifts in the choline resonance positions. Moreover, the Co(II) ions associated with the inner compartment could be fixed in space by precipitation of CoS after addition of H_2S. This resulted in changes in the NMR spectra, and the particles (often only 10–100 Å in diameter) could be imaged in real space by electron microscopy.

The development of the work relied not only on the newly introduced technique of electron microscopy [a similar dependence on instrumentation was associated with later work with regard to the method of proton-induced X-ray emission analysis (PIXE)], but on a stream of (to us) quite bizarre biological samples, provided by numerous collaborators [B. S. C. Leadbeater (SiO_2 in protozoa); M. D. Ross (inner ear crystals); R. P. Blakemore, R. B. Frankel, and T. T. Moench (magnetotactic bacteria); M. J. Hodson, C. H. O'Neill, and D. W. Parry (SiO_2 in grasses); P. Westbroek and E. W. de Jong (coccoliths); J. Webb (limpet teeth); R. F. C. Mantoura (acantharia); A. J. Brook (desmids); and A. R. Anderson (radiolaria)]. The importance of this wide-ranging collaboration and multidisciplinary approach was invaluable to the development of the chemical aspects of the research. It also furthered a bilateral approach, adopted also in this article, in which biological and synthetic (model) systems were often juxtaposed in a way that turned out to be very beneficial to the progress of the work.

For us, the most exciting part of the early stages of the work was the continual flow of ideas (usually written in indecipherable handwriting on the back of torn-off scraps of old manuscripts!), which regularly arrived on our desks. Most of these, it has to be said, were stillborn, and for all kinds of reasons ended up in the wastepaper bin. However, within such a multitude were ideas destined to become seminal. Look-

ing back, it was this somewhat turbulent, chaotic succession of ideas for which we are most grateful to Professor Williams. It engendered both a rigorous methodology (if only to keep them all in some sort of order!) and a confidence to view chemistry in new and diverse perspectives.

II. Biomineralization

A. Silica

In general, amorphous phases do not prevail in biology as these states are often much more soluble than their crystalline counterparts. This can be overcome only in systems in which unusual barriers to crystallization exist. One such example is hydrous silica ($SiO_2 \cdot nH_2O$), in which the kinetic barrier to crystallization is of the order of 800 kJ mol^{-1}, and amorphous phases, in which the Si—O—Si bond angle can have wide variations, are favored at low temperature and pressure. In terms of energetics, therefore, biogenic silicas are expected to be noncrystalline and this has been confirmed by infrared spectroscopy (*3*), electron diffraction, and ^{29}Si NMR spectroscopy (see below). In addition, high-resolution transmission electron microscopy (HRTEM) has been used as a means of studying the structural nature of biogenic silica. The great advantage of this technique is that it reveals structure directly and is therefore very appropriate for studying local architectural anomalies and structural microheterogeneities in amorphous materials. This is in direct contrast to the classical approaches of structural determination (X-ray, electron, and neutron diffraction), in which the volume of sample interacting with the incident radiation is microscopically large, yielding statistical data averaged out over the area analyzed.

The term "amorphous silica" encompasses an almost infinite variety of structural forms, from ordered opaline aggregates to extended gel-like materials. In all these structures, the mineral exists as a hydrated, covalent inorganic polymer of general formula $[SiO_{n/2}(OH)_{4-n}]_m$ (*4*). This formula, where $n = 0$ to 4 and m is a large number, indicates the variation in residual functional groups within the condensed structure. There is similar variation in the extent of hydration. This flexibility in composition and reactivity indicates that biogenic silica is not a stoichiometric mineral (in the way that $CaCO_3$ is, for example) and that the nature (density, hardness, solubility, viscosity) and composition of siliceous structures in biology may vary consid-

erably, being influenced directly and indirectly by a wide range of cellular processes.

Table I shows the distribution of silica in biological systems. In direct contrast to the abundance of siliceous structures observed in lower plants and animals, no silicified structures have been observed in bacteria. Why this should be so is not clear; however, because siliceous structures in unicellular organisms require the synthesis of special membrane-bound compartments, the lower structural organization of prokaryotic cells may be an important factor inhibiting the formation and organization of silica in these organisms.

In this section we review the structural and biochemical aspects of two contrasting biological systems involving silicification in (1) intracellular vesicles and (2) extracellular polysaccharidic matrices.

TABLE I

TYPES AND FUNCTIONS OF MAIN INORGANIC SOLIDS FOUND IN BIOLOGICAL SYSTEMS

Mineral	Formula	Organism/function
Calcium carbonate		
Calcite	$CaCO_3$[a]	Algae/exoskeleton; trilobites/eye lens
Aragonite	$CaCO_3$	Fish/gravity device; mollusks/exoskeleton
Vaterite	$CaCO_3$	Ascidans/spicules
Amorphous	$CaCO_3 \cdot nH_2O$	Plants/Ca store
Calcium phosphate		
Hydroxyapatite	$Ca_{10}(PO_4)_6(OH)_2$	Vertebrates/endoskeleton, teeth, Ca store
Octacalcium phosphate	$Ca_8H_2(PO_4)_6$	Vertebrates/precursor phases in bone?
Amorphous	?	Mussels/Ca store; vertebrates/precursor phases in bone?
Calcium oxalate		
Whewellite	$CaC_2O_4 \cdot H_2O$	Plants/Ca store
Weddellite	$CaC_2O_4 \cdot 2H_2O$	Plants/Ca store
Group IIA metal sulfates		
Gypsum	$CaSO_4$	Jellyfish larvae/gravity device
Barite	$BaSO_4$	Algae/gravity device
Celestite	$SrSO_4$	Acantharia/cellular support
Silicon dioxide		
Silica	$SiO_2 \cdot nH_2O$	Algae/exoskeleton
Iron oxides		
Magnetite	Fe_3O_4	Bacteria/magnetotaxis; chitons/teeth
Goethite	α-FeOOH	Limpets/teeth
Lepidocrocite	γ-FeOOH	Chitons (Mollusca)/teeth
Ferrihydrite	$5Fe_2O_3 \cdot 9H_2O$	Animals and plants/Fe storage proteins

[a] A range of magnesium-substituted calcites is also formed.

1. *Unicellular Organisms*

Stephanoeca diplocostata Ellis is a unicellular loricate choanoflagellate commonly found in coastal waters around Europe and the Mediterranean (*5*). The cells comprise a colorless protoplast with a single anteriorly directed flagellum surrounded by a ring of tentacles (the collar). The protoplast is lodged in an open-ended basketlike casing (lorica) constructed of 150–180 silica strips (costal rods) (Fig. 1). New costal rods are produced in advance of mitosis within long thin vesicles in the peripheral cytoplasm and are then released sideways through the plasmalemma so that, on cell division, the juvenile, taking the supernumerary strips with it as it leaves the parent lorica, is able to assemble its own basket within 2–3 min (*6*).

Chemical investigations of this biological system have attempted to address the following questions: (1) What is the microstructure of the hydrated SiO_2 within costal rods? (2) How are the costal rods linked together in the intact basket? (3) What is the nature of the surface silica in the costal rods? These questions were answered in some part by studies of intact and partially intact loricae, on demineralized costae, and by considering the nature of the interaction between metal ions (Fe^{3+}, Co^{2+}), colloidal silica, and liposomes with the costal strips.

HRTEM images of individual costal rods showed irregular incoherent fringes and no evidence of periodicity (*7*). No short-range order could be determined extending above 1 nm (approximately three Si—O—Si units), indicating that the silica comprised a continuous disordered gel-like structure. Moreover, the images indicated a structure based on a random network of SiO_4 units connected through Si—O—Si bonds of variable bond angle rather than a microcrystalline/cluster structure composed of a random array of microcrystalline polyhedra.

A final process in the assembly of the basket is the joining together of costal rods in a manner that allows the intact lorica to be resistant to forces arising in the marine environment. Figure 2 shows a junction between two costal rods and clearly indicates that the rods are glued together during the construction process. The connective material is generally less electron dense than the adjacent siliceous material of the costal strips. High-resolution electron micrographs have indicated that silica and probably organic material constitute the join (*7*). This suggests that the inorganic polymer has some residual flow properties that enable silica to move into the junction prior to hardening of the join.

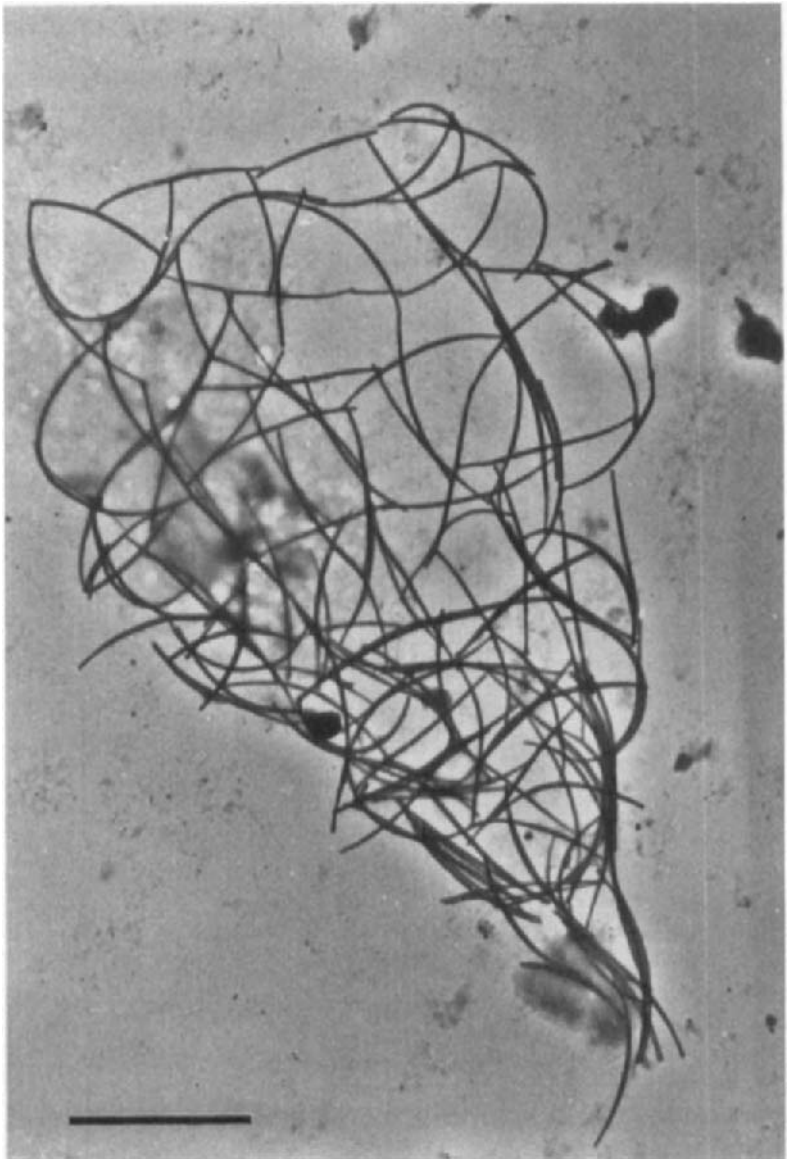

FIG. 1. TEM image of an intact lorica of *Stephanoeca diplocostata* Ellis. Bar = 5 μm.

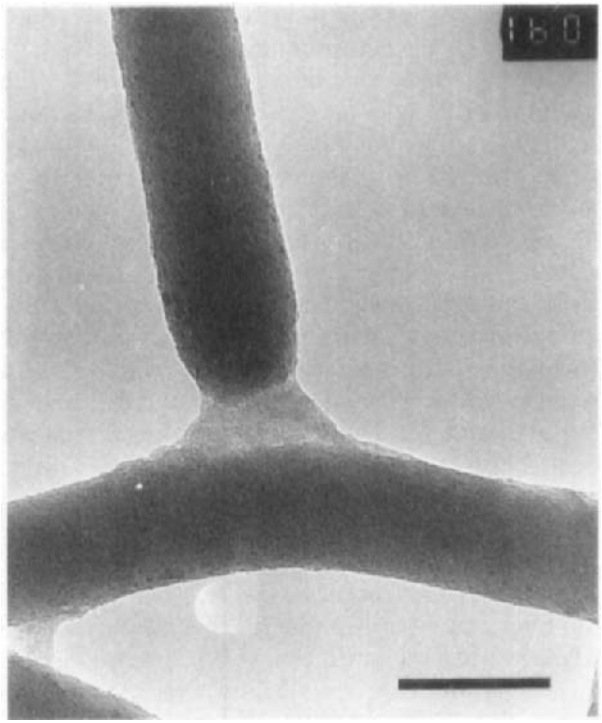

FIG. 2. Join between costal strips in the lorica of *Stephanoeca diplocostata*. Bar = 80 nm.

Interestingly, the silica-containing costal rods are metastable and slowly redissolve in the aqueous medium. The process of demineralization depends on the conditions of physical growth; at 20°C in an agitated solution, demineralization is complete within 10 days (*8*). Studies of silica demineralization have been important in revealing differences in the local chemical environment of silica within the costal rods. The initial stage of demineralization takes place at localized centers along the central axis of the strip, suggesting that these regions comprise silica that is more hydrated (soluble). Alternatively, the surface silica may be preferentially protected by an organic membrane. The initial centers become increasingly demineralized with time until they extend and join together along the central axis, forming tubular, brittle rods. As demineralization increases, the hollowing becomes more extensive and only at the later stages do the outer edges of the costal rods show signs of demineralization, becoming rough and pitted. An interesting implication of this preferential dissolution is that the

rods become hollow without significant reduction in their mechanical strength (compare the use of tubular steel rods in building scaffolding). Thus the silica basket remains functional, i.e., intact, even though the costal strips have undergone extensive demineralization. Only when the tubular walls become very thin does fracture and buckling occur. The mechanical design of biogenic silicas is therefore an important consideration in relating structural properties to biological function.

Although the detailed nature of the surface of costal strips is not known, evidence from binding studies indicate that cations such as Co^{2+} and Fe^{3+} are preferentially adsorbed onto these structures (*9*). Similar interactions have been shown with organic and colloidal materials (*9*). For example, phospholipid vesicles were shown to be closely attached to the surfaces of costal rods incubated in aqueous dispersions of phosphatidylcholine for 24 hr. Similar observations were made for costal rods incubated in solutions of colloidal silica. These results indicate that a range of interactions can take place on the surface of biogenic silica and such events may serve important functional roles, such as inhibition of dissolution and adhesion of components in the construction of microscopic structures.

One of the major unresolved questions is how this molecularly isotropic material is fabricated into elongated curved rods. During mineralization, the rods remain surrounded by a vesicle membrane that lies in association with two microtubular filaments (*8*), suggesting that the shaping of the vesicle by cellular stresses may be responsible for the elaborate morphology of the mature mineral particles. Deposition could take place in several ways. Silicification could be the result of a specific binding mode for silicic acid within the vesicles, followed by localized polymerization. Binding of silicic acid to organic molecules can occur through hydrogen bonding, ionic interactions, or condensation of OH groups (*10*). Alternatively, an energized dissolved silica concentration gradient within the vesicles could initiate silicification through changes in osmotic pressure, pH, or concentration. Concurrent with silica deposition must be biochemical processes involving regulation of silicic acid metabolism and control over the organic components involved in vesicle development. A more general overview of the mechanisms underlying biosilicification is given in Section II,A,3.

2. *Higher Plants*

Siliceous plant fibers from *Phalaris canariensis* L. (canary grass) (and others of the same family) have been implicated in the etiology of esophageal cancer in certain regions of the world (*11*). These fibers are considered to act in the same way as asbestos fibers in causing cells to

grow abnormally around the elongated mineral particles. The biogenic fibers were derived from hair cells on the outer surface of plant seeds. Viewed in polarized light, the silica fibers were birefringent and were assumed to be crystalline (*12*). As this was highly unlikely, because of the high activation energy barrier to crystallization, we undertook to investigate the nature of this siliceous material that is found in conjunction with an extracellular polysaccharide cell wall matrix.

At the molecular level the silica contained tetrahedrally coordinated silicon atoms in a wide range of environments as judged by the peak widths of resonance positions obtained by solid-state ^{29}Si NMR spectroscopy (*13*). The silica contained $Si(OSi{=})_4$ (Q4), $Si(OSi{=})_3(OH)$ (Q3), and $Si(OSi{=})_2(OH)_2$ (Q2) species. The proportions (Q4 : Q3 : Q2) as measured by peak deconvolution techniques were 68 : 22 : 8% (Fig. 3), with the proportions varying little among samples containing silica only and those containing the polysaccharidic cell wall matrix. The use of trimethylsilane enabled the measurement of surface available silanol groupings for the silica-only sample (*4*). A high proportion of the silanol groups was not accessible to this reagent, suggesting that the internal structure of the silica phase was not totally anhydrous. No Si—O—C covalent bonds were detected in the native samples, although spectral data obtained from cross-polarization experiments of both cell wall and silica-only samples showed that the organic matrix was sufficiently close in space to act as a pathway for efficient relaxation of silicon nuclei (*14*).

HRTEM showed that the material was amorphous at the nanometer

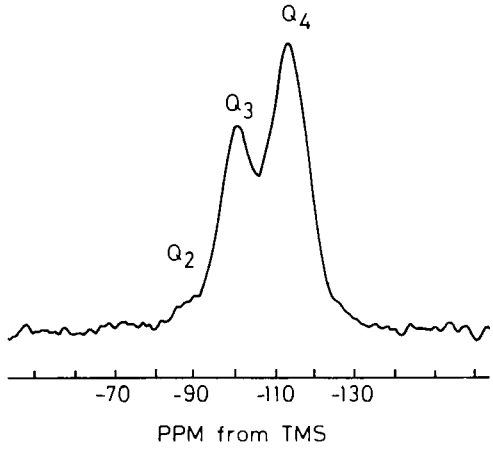

FIG. 3. ^{29}Si solid-state NMR spectrum for plant silica. Q_4, $Si(OSi{=})_4$; Q_3, $Si(OSi{=})_3OH$; Q_2, $Si(OSi{=})_2(OH)_2$. TMS, Tetramethylsilane.

level, the lattice images being very similar to those reported for *S. diplocostata* Ellis (*7*). However, low-resolution images showed, to our great surprise, that the microsopic form of the silica in the plant hairs was very different from that found in the protozoan system described above. The plant silica was particulate in nature and secondary structural motifs were built up from primary particles of different sizes, shapes, and surface chemistries (Fig. 4) (*15*). The structures observed were classified as sheetlike, globular, and fibrillar depending upon the nature of the aggregation between the particles. The range of particle sizes observed in a particular structural motif was limited. Apart from globular structures wherein small (5–10 nm) particles coalesced to produce larger particles, all the other motifs were built up from clearly distinguishable particles that remained distinct from one another under conditions of analysis. Ill-defined areas, including necked particles, were not observed. The stability of the structural motifs in the electron microscope was considerable, in comparison to industrially prepared precipitated silicas of similar dimensions.

An initial indication of surface hydroxylation was provided by consideration of sample stability in the electron beam, with fibrillar particles being least stable, globular structures being of intermediate stability, and the sheetlike particulate arrangement being most stable. More recently, a method of qualifying this behavior has been obtained by development of surface-specific stains for use in the electron microscope (*16*). The method employed the use of bis(cyclopentadienyl)titanium dichloride as a surface silanol-staining agent. UV spectropho-

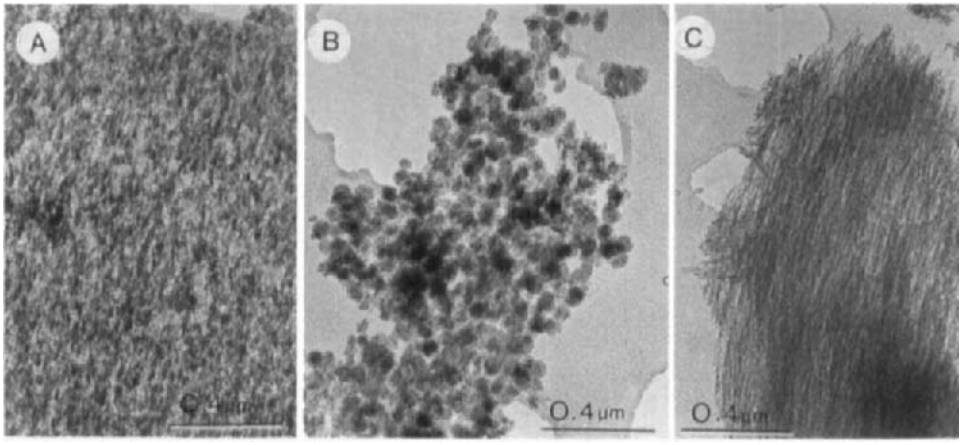

FIG. 4. Examples of structural motifs exhibited by plant silicas extracted from macrohairs of *Phalaris canariensis*. (a) Sheetlike, (b) globular, and (c) fibrillar.

tometry of solutions was used to follow the course of the surface reaction, and electron microscopy was used to obtain information on the relative Ti/Si concentrations for different substructural types. Both procedures gave an indication of the percentage of available hydroxyl groups in the different silica motifs.

The chemistry of the process involves an initial surface reaction,

$$]\text{—Si—OH} + Cp_2TiCl_2 \rightarrow]\text{—Si—O—}TiCp_2Cl + HCl$$

while further reaction may be possible, e.g.,

$$]\text{—SiOH} +]\text{—SiO}TiCp_2Cl \rightarrow]\text{—Si—O—}TiCp_2\text{—O—Si[} + HCl$$

if the silanol groups are in close proximity. The results showed that the plant silica substructures had a range of levels of reagent uptake and the number of surface silanol groups was higher than for industrial silicas prepared by a range of preparative routes. In addition, silanol concentrations varied for structural motifs within a single hair cell and for similar structural motifs found in different biological samples. Further experiments are aimed at the design of heavy-metal-containing reagents for reaction with specific geometric hydroxyl groupings such as isolated, geminal, and vicinal silanols.

An immediate question that arose from the observation of different structural arrangements was whether the motifs were located in particular regions of the plant hairs. Careful analysis of fractured plant hairs showed that sheetlike material was deposited at the outer regions of the hair, followed by globular silica with fibrillar silica being deposited around a central axial hole (*15*). Analysis of two-dimensional images was not entirely satisfactory and studies on silica precipitated during the development of the hairs provided additional evidence for sheetlike silica being deposited prior to globular silica, with fibrillar silica only being deposited at a very late state in the mineralization process (*17*). Studies on other plant hair systems, including the stinging hairs from *Urtica dioica,* the common stinging nettle, have shown similar structural motifs (*14*, *18*). The pattern of deposition was similar to that described above, but, in addition, smectic and globular/fibrillar structures were precipitated during the early stages of silicification and platelike and fibrillar motifs were only deposited as the system reached maturity.

Studies of particulate silicas from heavy silicon accumulators such as the horsetail plant, *Equisetum arvense,* have shown that various parts of the plant deposit principally single motifs (*19*). In the primi-

tive leaves of this plant, globular silica is observed, whereas in the internodal regions, fibrillar silica is the most typical motif observed. The nodal regions comprise both globular and fibrillar material and for the leaf sections closest to the stem a small amount of fibrillar material in addition to the globular motif is observed. These observation may be correlated with rate of water flow through various regions of the plant.

3. Mechanisms in Biosilicification

The structural organization of biogenic silicas depends on the regulation in time and space of physicochemical processes within the mineralization environment. A siliceous structure will develop from a series of molecular events that involve nucleation and growth (polymerization) processes. Biology is able to manipulate the polymerization and depolymerization of silica by chemical and biochemical processes at the mineralization site to produce structures with functional form. The presence of discrete particle sizes and hydration stability can result from a combination of factors, including (1) time-dependent local Si concentration effects (complexation, pH, etc.), (2) temporal and spatial variations in the concentrations of ionic species, and (3) the prevention of dissolution/reprecipitation phenomena by the presence of hydrogen-bonded polymers coating preformed particle surfaces and/or the removal of water from the site of deposition. Clearly, in trying to ascertain the relative importance of factors involved in the formation and stabilization of certain particle types, it is important to characterize the bulk and surface chemistries of the individual particle types, including any interaction with organic macromolecules.

a. Chemical Control by Inorganic Components. The importance of the ionic environment as a morphology regulator for the deposition of silica is well documented (*20*). Structural studies of both macrohairs from *P. canariensis* and stinging hairs from *U. dioica* have shown that morphologically distinct silica structures are deposited at precise times and in well-defined locations within these plant hairs. In parallel with structural studies, energy-dispersive X-ray analysis (EDXA) and scanning proton microprobe (SPM) analysis have been used to study changes in elemental distributions and concentrations in the developing macrohairs (*15, 18, 21*). Used together, these techniques have provided valuable insights into the involvement of cellular activity in biomineralization and in the identification of distinct chemical zones of mineralization.

The application of the Oxford scanning proton microprobe to these studies was of particular importance in the monitoring of trace ele-

ments that could not be reliably measured using EDXA. The ability to focus the high-energy (4 MeV) proton beam down to a diameter of 1 μm using quadrupole lenses (*22*) while maintaining a beam current of the order of 100 pA enabled reliable mapping of trace elements. Both EDXA and SPM analysis on immature hairs have shown that silicification commences at the tip of the hairs (Fig. 5). SPM data showed that K was concentrated behind the initial deposit of silica and was also present at lower levels throughout the entire macrohair. Low levels of P and S were also detected along the length of the hair. The presence of considerable quantities of K, Cl, P, and S within immature hairs indicated that cellular contents were present during the early stages of silicification. SPM studies on mature hairs and studies of sectioned material (*23*) indicated that withdrawal of cellular contents occurs during silicification. Although K, Cl, and P were not present in mature cells, a continuing low level of S in the hairs suggested involvement with membranous structures within the organic component of the silicified cell wall.

The temporal and spatial localization of specific inorganic elements during mineral deposition suggests that silicification is closely connected with underlying cellular processes that may ultimately control the aggregation of microscopic silica particles from supersaturated silicic acid solution. The presence of trace levels of ions throughout the mature hairs suggests possible involvement in the neutralization of surface charges on initially formed silica particles, thus aiding aggregation. In studies of nettle hairs, which contain both silica and calcium

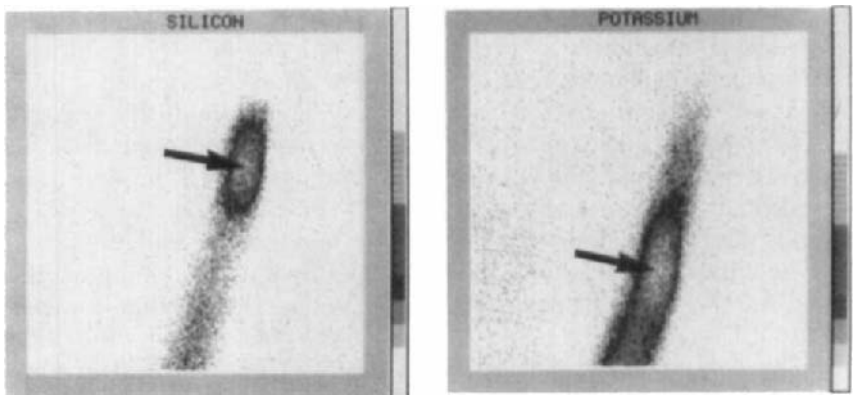

FIG. 5. Elemental SPM maps of a hair tip (*Phalaris canariensis*) 4 days after emergence of the inflorescence. Total area scanned was 60 μm. Silicon is concentrated at the tip with high local concentrations of potassium directly behind the tip.

oxalate at maturity, silicification commenced when the hairs were only 5% of their final length; for this system silicification is virtually complete by the time calcification begins (*18*).

It is known that the growth of silica is governed by interfacial processes. Organic and inorganic (ionic) components may moderate the mineralization process. High levels of ionic activity (0.2–0.3 *M* Na^+ and K^+) may promote particle aggregation due to surface charge reduction between primary silica particles, but do not (on their own) regulate the development of morphological features. It is important to note that at no time during silica deposition were significant levels of Ca^{2+}, Mg^{2+}, or Fe^{3+} detected. This could be considered surprising, as highly charged cations have a significant effect on aggregation in synthetic systems involving silica deposition. Hydrogen bonding "flocculants" such as alcohols, proteins, lipids, and polysaccharides may also promote particle aggregation, but only when ionic concentrations are low. It is possible, therefore, that subtle changes in the chemistry of the local environment can determine the distinctive morphological forms of biogenic silicas.

b. Organic Matrix Control. Silica deposition in plant hairs occurs in the cell wall, wherein polysaccharides make up the bulk of the structure. Radiochemical labeling studies on hairs from the lemma of the grass *P. canariensis* have shown that silicification commences after cell growth is complete and primary cell wall synthesis has ceased (*17*). At the early stages of development, arabinoxylans and cellulose are principally synthesized at the same time that sheetlike silica is deposited. At later stages of development, the relative rates of synthesis of cellulose and arabinoxylans decrease in importance and the rates of synthesis of noncellulosic mixed-linkage $\beta(1-3)$ and $\beta(1-4)$ glucans increase in importance. This phase is associated with globular silica deposition. Fibrillar silica is deposited only during the latter stages of cell development and is incorporated into and associated with a mature organic matrix in which synthesis of secondary cell wall material has ceased. The importance of matrix structure on silica structural components is not fully understood, but it is feasible that the polymers could provide different spatial environments and hydrogen bonding centers for interaction with the developing silica phase. Direct bonds between the organic and inorganic phases of various silicified systems, including plant components, sponges, diatoms, and limpets, however, have not been detected by ^{29}Si NMR spectroscopy (*24*).

Evidence to substantiate the view that direct interactions do exist among organic polymers and biogenic silica comes from studies of se-

lective enzymatic carbohydrate degradation studies on silicified and desilicified plant hair samples (*14*). Silicified and desilicified hairs from *P. canariensis* and *U. dioica* were treated with a range of enzymes, including xylanases, cellulases, and driselase, which contains a mixture of fungal hydrolases. For both plant systems the action of the cellulase was barely affected by the presence of silica. For the other enzyme systems investigated, the presence of silica within the cell wall matrix was found to confer a marked reduction in the susceptibility of other cell wall polymers to attack by wall-degrading enzymes typically produced by plant pathogens. Treatment with zylanase I and II led to a preferential release of arabinose and xylose from desilicified cell walls and treatment with driselase led to a preferential release of glucose with a smaller increase in arabinose liberation. Comparative studies with largely nonsilicified plant hair cells showed no difference in saccharide release even after HF treatment (used to remove SiO_2 from the silicified samples). The data appear to indicate that silica acts to protect cell wall polymers from attack by enzymes released by pathogenic organisms. The preferential release of certain monosaccharides after silica removal suggests that certain polymers, possibly side chain components of arabinoxylans or glucans, are more intimately associated with the siliceous phase than are other polymers. Current experimentation on this system involving double labeling of the polysaccharide phase (^{14}C) and silica phase (Ge) is aiming to define more precisely which biopolymers are synthesized in association with particular silica structural motifs.

c. Mechanical Stress Controls. The packing of biogenic silica may be controlled by the principles of flow ordering. On studying small particles (e.g., sand) in a flowing stream, it is observed that where the flow is unidirectional in the center of the stream, the particles appear close packed. Toward the edge of such a stream, where the flow is perturbed, particles are arranged in a much less ordered fashion, for example, swirls, due to vortices in the flowing liquid. The packing of silica particles in many biological systems may be more closely related to the principles of flow ordering than to packing on an adherent (epitaxial) surface.

We have observed in various kinds of plant hairs that silica particles are packed around a central axial channel, which at the early stages of development contains cytoplasmic material and a large vacuole, which is the likely pathway for water flow. An explanation for the structural motifs observed could proceed as follows: Along the inner edge of this cylinder the silica appears closely packed (fibrillar) and ordering is

along the length of the cylinder in the proposed line of flow. Further from this central region the organization of fundamental silica particles is distinctly more disorganized and a globular motif is observed. The space available for the silica particles within the developing cell wall will restrict the size of the particles that can form. Sheetlike material, deposited at the early stages of mineral formation, is not as well ordered as the fibrillar material and is not oriented in line with the proposed direction of flow. The directional nature of this structural motif may result from a closer adherence to the organic cell wall, compared to the other structural motifs within the plant hair system. A similar phenomenon is observed for silica deposition in the multicellular plant *E. arvense,* for which it is proposed that silica particles may not be formed *in situ* but may be nucleated within the transpiration stream and transported to their final site as they ripen. In regions of high water flow (internodes), fibrillar material is observed and in regions of little water flow (leaves) globular motifs are observed. For this primitive plant, the shapes and biochemical characteristics of the individual cells within the stem and the leaf, as well as the importance of water flow, may be important factors in determining the morphologies observed.

B. Iron Oxides

In contrast to biogenic silica, both crystalline and amorphous iron oxides are deposited in biological systems. Only recently has the phenomenon of iron oxide biomineralization been studied in depth. It is now known that iron oxide formation in organisms is widespread, having been reported in all five kingdoms ranging from animals to bacteria (Table I). Thus the central role played by Fe in conventional bioinorganic chemistry is mirrored in the important biological function of this element in the solid state. In general, structural studies of biogenic iron oxides have been successful in elucidating the crystallographic structure, degree of order, morphology, and crystal growth mechanisms of these intriguing materials. Here we highlight the importance of bioinorganic studies in the investigation of (1) magnetite (Fe_3O_4) synthesis in magnetotactic bacteria and (2) ferrihydrite formation ($5Fe_2O_3 9H_2O$) in the iron storage protein, ferritin.

1. Magnetite in Magnetotactic Bacteria

Life on earth has evolved under the influence of the earth's magnetic field and, perhaps not surprisingly, some organisms are thought to have adapted such that they can detect and exploit this phenomenon.

In this regard, the discovery of a very simple magnetotactic response in certain species of bacteria was of profound importance (*25*). These bacteria orient and swim along geomagnetic field lines and have a direction of magnetic polarity such that they swim exclusively downward in both the Northern and Southern Hemispheres (*26, 27*). Electron microscopic examinations have shown that the bacteria contain intracellular inclusions of Fe_3O_4, which are enveloped by a membrane and localized in chains in close proximity to the inner surface of the cytoplasmic membrane (*28, 29*). The magnetite particles are in the single magnetic domain size range such that a chain of the crystals imparts a sufficiently strong permanent magnetic moment to orient the bacteria in the geomagnetic field (*30*).

a. Structural Studies. The structure of magnetic particles extracted from a range of bacteria such as coccoid (*31*), vibrioid (*32*), and spirillum-type cells (*33*), as well as from algae (*34*), has been determined by electron diffraction. The data clearly identify the biogenic mineral as magnetite (Fe_3O_4) but are not intrinsically accurate enough to give confident values of the unit-cell parameter to more than two decimal places. Moreover, because of the relatively large inaccuracy in electron diffraction data, it is difficult to distinguish the small differences between magnetite *d* spacings and those of the related cation-deficient orthorhombic spinel γ-Fe_2O_3 (maghemite). Although ^{57}Fe Mössbauer spectroscopy can clearly distinguish between these two minerals, the amount of material required is often much greater than that experimentally available. As a consequence, the only bacterial magnetites studied to date by Mössbauer spectroscopy are from *Aquaspirillum magnetotacticum* (*35*) and the marine vibrioid MV-1 (*36*); the data show conclusively that in these organisms the magnetic biomineral is in the form of stoichiometric magnetite.

HRTEM studies (*31–33, 37, 38*) have confirmed the single-crystal nature of individual bacterial magnetite inclusions. Lattice fringes recorded on individual mature particles were well-defined, continuous, and regularly spaced throughout the inclusions (Fig. 6). Few structural irregularities such as stacking faults and dislocations were observed, indicating that the crystals are formed by highly controlled crystal growth processes. Furthermore, many magnetotactic bacteria organize their magnetite crystals into chains that often run parallel to the long axis of the cell. The crystals are crystallographically oriented such that the [111] axis lies parallel to the direction of the chain (*33*). This arrangement may have functional value because the [111] crystal axis is also the easy axis of magnetization in magnetite. The latter

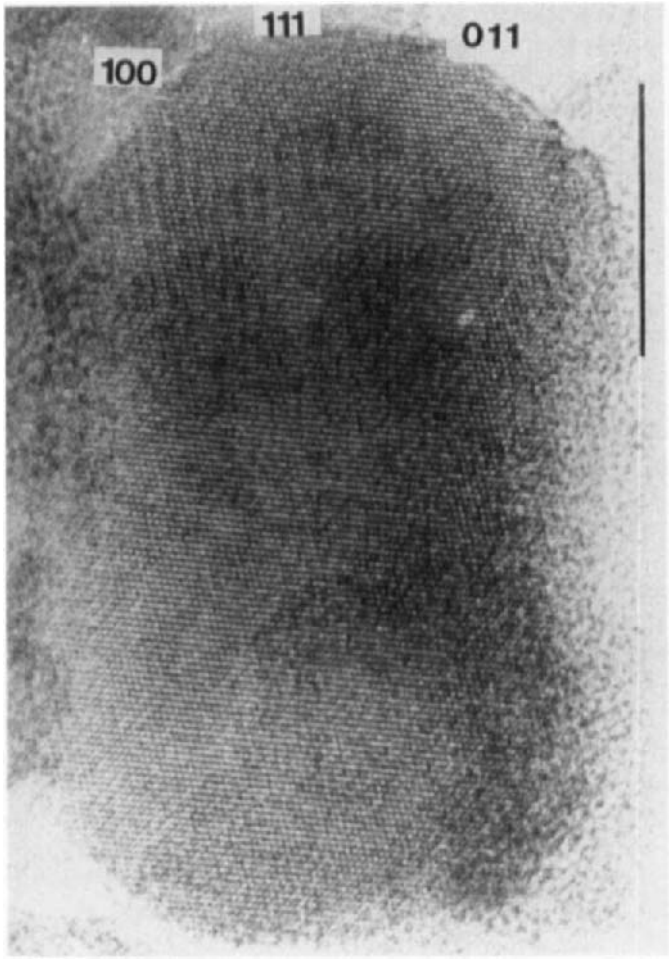

FIG. 6. HRTEM lattice image of a bacterial magnetite crystal from coccoid cells. The crystal is imaged along the [110] direction and has a characteristic rectangular shape when viewed in projection. Truncated faces are identified. Lattice fringes are {111}, 4.85 Å and {200}, 4.2 Å. Bar = 20 nm.

corresponds to the direction along which the electron spin can be more readily coupled and hence is the optimal direction for the organization of an interacting assembly of magnetic crystals functioning as a sensor of field direction.

b. Morphological Studies. Low-magnification electron micrographs of bacterial magnetite indicate a variety of morphological

forms that are species specific (*39*). Viewed in projection, cubic, rectangular, hexagonal, and bullet-shaped particles have been observed (Fig. 7). The true three-dimensional morphology has been established through the identification of different sets of lattice spacings and their corresponding angular relations within crystals oriented along a range of different crystallographic directions. However, the conclusions refer only to idealized crystal morphologies, because many biogenic crystals exhibit local distortions in shape that are difficult to rationalize in terms of crystal symmetry.

The simplest morphological form is that exhibited by crystals synthesized in *A. magnetotacticum*. Lattice images indicated that these

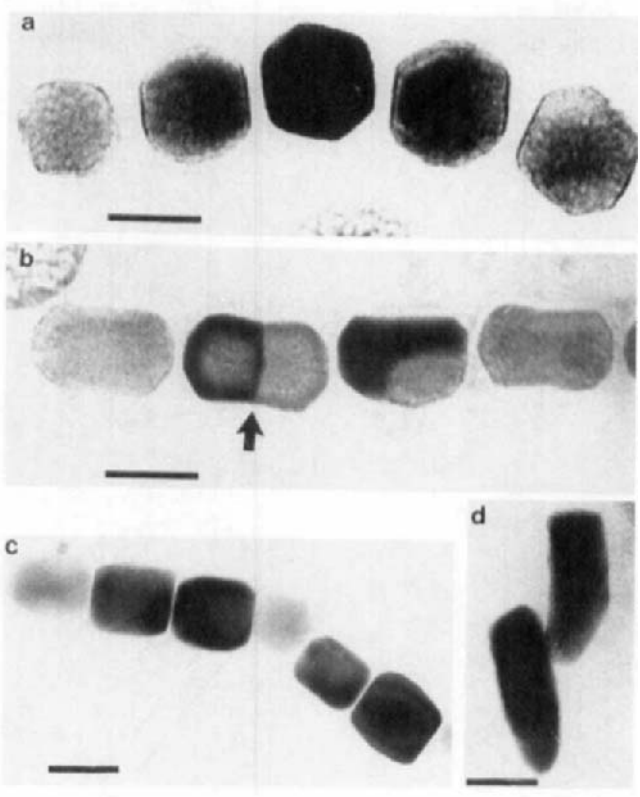

FIG. 7. Morphological forms of bacterial magnetite observed in projection. (a) Hexagonal (cubo-octahedral); (b) rectangular [note the twinned crystal (arrow)]; (c) cubic; and (d) bullet shaped. In each case the crystals are oriented with the (111) faces perpendicular to the chain axis. Bars = 50 nm in all micrographs.

crystals are cubo-octahedral in shape (Fig. 8a). This crystal habit is the equilibrium form common in inorganic magnetite and reflects the stability of the close-packed octahedral {111} faces and the strongly bonded cubic {100} faces. A similar analysis of magnetite crystals formed in coccoid cells showed that the rectangular morphology of these crystals, when viewed side-on at low magnification, is the projection of a truncated hexagonal prism. In one coccus type (*31*), the hexagonal prism is capped by only one of the four symmetry-related {111} sets and the other {111} faces are not expressed in the crystal morphology (Fig. 8c). Furthermore, the crystal is preferentially elongated along one of the four [111] axes. A similar discrimination is made with regard to faces of index {110}. Six of the 12 symmetry-related {110} faces are extensively formed as the elongated sides of the hexagonal prism, whereas the remaining six are expressed as small truncated

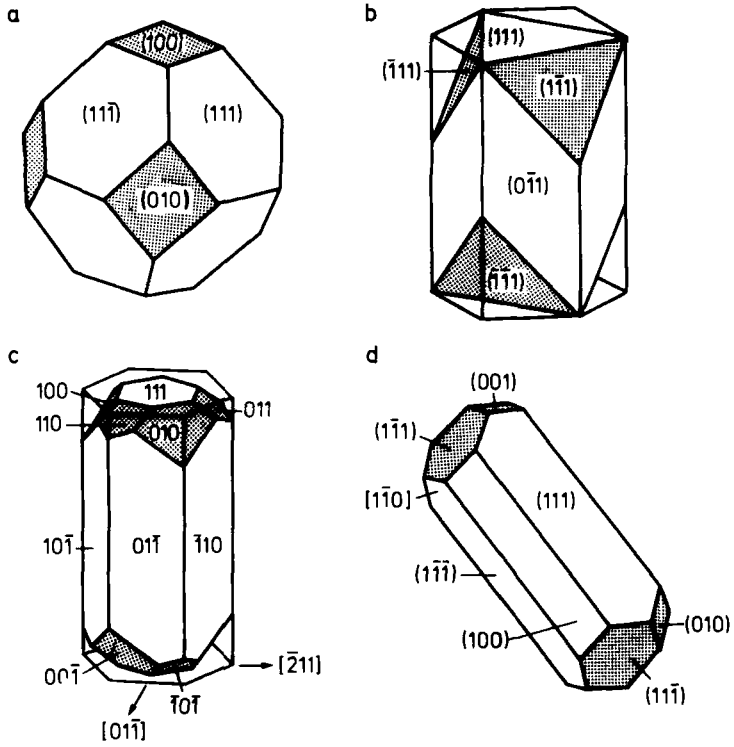

FIG. 8. Idealized crystal morphologies of bacterial magnetite. (a) cubo-octahedron (*Aquaspirillum magnetotacticum*); (b and c) hexagonal prisms (coccoid and vibrioid cells); (d) elongated cubo-octahedron (wild-type cells).

faces at the ends. A related hexagonal habit has been determined for magnetite crystals synthesized in the cultured marine vibrioid MV-1 (*32*). The lattice images clearly indicated that both the top and truncated side faces are of {111} form and the crystals had a hexagonal cross-section comprising six {110} faces (Fig. 8b). Matsuda *et al.* (*37*) have obtained similar results in an unspecified coccus cell type.

An extreme example of this apparent biological preference for hexagonal magnetite habits has been observed in wild-type bacterial cells synthesizing single-domain bullet-shaped crystals (*38, 40*). These crystals exhibit an elongated cubo-octahedral form comprising a hexagonal prism of {111} and {100} faces, capped by {111} faces and with associated {111} and {100} truncations (Fig. 8d). In many crystals the axis of elongation lies parallel to the [112] crystallographic axis and, again, there is differentiation of symmetry-equivalent faces.

The cubo-octahedral and bullet-shaped crystals are closely related even though in the final product they appear to be very different. At the early stages of development, the bullet-shaped crystals are isometric cubo-octahedra (*40*) and subsequent growth is therefore primarily constrained in one direction, resulting in the elongated crystals. The elongated hexagonal crystals, however, are fundamentally different. Although a range of truncated faces may be expressed (see above), these crystals appear to develop anisometrically very early on in the mineralization process. Furthermore, they remain centrosymmetric throughout their growth.

c. Crystal Growth. The investigation of the processes of crystal growth of bacterial magnetite has focused on structural studies of immature crystals because the crystallochemical properties of these crystals reflect the intrinsic mechanisms of crystal synthesis. Crystals from *A. magnetotacticum* at early stages of growth have been studied *in situ* by HRTEM (*33*). Although smaller crystals often appeared to be located at the ends of the chains, no linear sequence of crystallographic development along the chain could be determined. Thus, both well-developed and irregular particles were often observed adjacent to each other. Lattice imaging of the immature irregular particles showed the presence of contiguous crystalline and noncrystalline regions within the magnetosomes. The crystalline zone was always observed to be single domain with well-ordered lattice planes of magnetite. The lattice fringes often appeared to extend into the amorphous region in a preferential direction, which may indicate a preferred nucleation and growth direction. These data are in agreement with ^{57}Fe Mössbauer studies of frozen whole cells that showed the presence of a high-spin

Fe(III) component in addition to magnetite in spectra recorded at room temperature (*35*).

As with *A. magnetotacticum,* amorphous hydrous iron(III) phases have been observed by HRTEM in wild-type cells (*38*) and coccoid cells (*31*). However, direct evidence for their involvement at the nucleation or early growth stage of magnetite development is lacking. Crystals at intermediate stages of growth in coccoid cells show characteristic rounded edges and irregular, structurally disordered surfaces. These observations suggest that growth of the crystals occurs through surface-mediated reactions involving the phase transformation of ferrihydrite to magnetite. There is similar evidence for the involvement of surface-adsorbed iron(III) phases in magnetite growth in wild-type cells (*38*). Amorphous regions and structural irregularities were imaged only at the tapered end of the bullet-shaped crystals, indicating that this face represents the growth front in the anisotropic development of these magnetosomes.

d. Mechanisms of Magnetite Biomineralization. On the basis of HRTEM, Mössbauer spectroscopy, and biochemical results, a sequence of events leading to bacterial magnetite can be proposed. These involve (1) uptake of iron(III) from the environment via a reductive step in membrane transport (*41*); (2) transport of iron(II) [or iron(III) as ferritin?] to and across the magnetosome membrane; (3) precipitation of hydrated ferric oxide within the magnetosome vesicles; (4) phase transformation of the amorphous iron(III) phase to magnetite both at the nucleation stage and during surface-controlled growth.

The organization and ultrastructure of the surrounding magnetosome membrane is fundamental to the control of magnetite biomineralization. This membrane, which has an overall composition similar to other cell membranes, contains two proteins (*42*) that may be specific to the nucleation and growth of magnetite. The formation of the enclosed vesicle appears to occur prior to mineralization and provides both a spatial constraint for growth and a defined chemical reaction volume via selective ion transport. Furthermore, the presence of a charged organic surface may be an important factor in determining the kinetics and structural characteristics of the nucleation event.

The single-crystal nature of the majority of bacterial magnetites implies that nucleation of magnetite from the iron(III) precursor phase occurs at one primary nucleation site that grows at the expense of other potential sites. It is probable, therefore, that the surrounding magnetosome membrane plays a crucial role in the generation of a local environment for site-directed nucleation. One possibility is that

protein molecules, active in nucleation, are spatially organized at a unique site in the membrane, and all other potential sites are deactivated by inhibitor molecules located within the vesicle. Furthermore, because the crystals are preferentially oriented with the {111} face perpendicular to the chain axis, it seems probable that the membrane exerts a degree of crystallographic control on the magnetite face that is nucleated adjacent to the organic surface.

The phase transformation of amorphous hydrated ferric oxide to magnetite can occur at neutral pH provided the redox potential of the reaction environment is of the order of −100 mV (*43*). The redox potential will be extremely sensitive to pH such that small changes in $[H^+]$ could have marked influence on the phase transformation processes. The rate of transformation of hydrated ferric oxide to magnetite is likely to be slow, as dehydration, dissolution, reprecipitation, and partial reduction of iron(III) are involved. Investigations of the transformation of ferric oxides to magnetite under aqueous conditions in inorganic systems have shown that the critical step is the involvement of aqueous iron(II) at the ferric oxide surface (*44*). A two-step process is postulated (Fig. 9). The rate of magnetite formation appears to be essentially first order with respect to the concentration of the surface intermediate formed in step 1. Although the composition of the intermediate released into solution is unknown, the formation of Fe_3O_4 in the second step involves the release of one further proton. The resultant lowering in the reaction pH and subsequent increase in redox

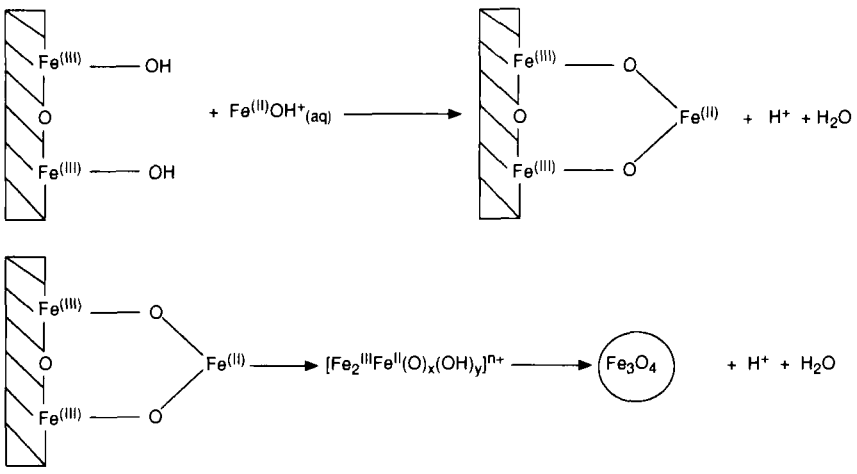

FIG. 9. Two-step reaction sequence for magnetite synthesis from the reaction of aqueous iron(II) with ferrihydrite.

potential imply that for the phase transformation to magnetite to proceed to any significant extent within the magnetosome vesicle, there must be precise regulation of the pH and hence redox potential within the localized mineralization zone.

On the basis of these *in vitro* observations, it seems probable that the immature bacterial crystals develop through phase transformation processes involving a solution interface between the crystalline and amorphous phases. Initially, the amorphous phase is the kinetically favored product resulting from iron(II) oxidation. Continual flux of iron(II) across the magnetosome membrane will result either in additional ferric oxide formation or reaction of iron(II) with the preexisting iron(III) phase to give magnetite within the vesicle. The second pathway becomes competitive with a continual increase in iron(II) influx.

One of the most surprising aspects concerning the shape of bacterial magnetite crystals is the predominance of anisotropic forms compared to the isotropic habits of inorganic origin. Thus the elongated morphology of bacterial magnetites must reflect some fundamental feature of the mechanism of biomineralization. The concept of an imposed spatial constraint is applicable to the growth of bullet-shaped magnetites in wild-type cells. Development of the crystals takes place in two distinct stages (*38*). The first stage involves the development of isotropic magnetite crystals, of cubo-octahedral morphology, which grow to a size of 20 nm. There is no spatial constraint imposed on crystal growth at this stage because the crystal grows out from the membrane wall equally in all directions. The second stage involves anisotropic growth along the [112] direction, resulting in three of the {111} and {100} planes becoming elongated. One can envisage that the crystals grow either within preformed elongated vesicular sacs or in vesicles that are continuously being extended along a preferential direction (perhaps parallel to the cell membrane) during crystal growth. Thus the cytoskeletal organization of the vesicular system may be of primary importance in morphological specificity, as it is in the formation of curved silica rods in protozoa (Section II,A,1) and the development of $SrSO_4$ spicules in acantharia (Section II,C,2). However, there is a fundamental difference here between the crystalline and amorphous systems, because a passive role for the membrane does not explain the preferential crystallographic alignment of the magnetite within the elongated vesicle. The crystallographic orientation of the crystals is established at the nucleation stage through specific formation of the {111} face on the immobile wall of the expanding vesicle. In this process the orientation set by the nucleation interactions must be coupled to the axis of unidirectional growth and vesicle elongation.

A different mechanism of anisotropic growth appears to be present in the coccoid and MV-1 crystals. The crystal habit of these particles (Fig. 8b and c) appears to be established not via the spatial restriction of a growing isotropic crystal, but as an intrinsic property of the initial crystals nucleated within the magnetosome vesicles. Although specific molecules present within this environment could give rise to novel crystal habits, one would predict that these would remain isotropic, because the activity of growth mediators is equivalent on symmetry-related surfaces. One possibility is that the spatial organization of ion-transport centers on the magnetosome membrane generates different growth rates of symmetry-equivalent directions because the flux of ions to the crystal surfaces is highly directional. Thus the hexagonal prism morphology could be related to a three-fold symmetry of transport centers on the membrane and elongation could arise by a greater flux rate in the axial direction. Moreover, vectorial crystal growth would be enhanced if the membrane and crystal surfaces were in direct contact throughout crystal growth such that the lateral diffusion of ions in solution was minimized.

2. *Ferrihydrite Mineralization in Iron Storage Proteins*

The storage and mobilization of surplus iron in eukaryotes and some prokaryotes are regulated by the iron storage protein, ferritin. Ferritin isolated from horse spleen consists of a hollow spherical shell of 24 symmetrically related protein subunits (~18 kDa per subunit) surrounding a core of inorganic hydrated iron(III) oxide (*45*). Phosphate may be associated with the surface of the iron oxide core in horse ferritin, but does not appear to be a critical factor for core formation in reconstituted ferritins (*46*). The diameter of the cavity set by the protein shell is of the order of 70–80 Å, resulting in an upper limit of 4500 iron atoms (~30% wt/wt Fe) that can be stored within the molecule.

The uniqueness of the ferritin structure arises from the metabolic requirement to organize and utilize dissolved iron at concentrations and pH levels that induce precipitation of potentially toxic solid phases. Not only is iron solubilized by micelle encapsulation, but homeostatic control is also maintained. The study of ferritin therefore provides an important example of biological control of solid state reactions that involve the formation and organization of nanometer-size inorganic solids in biological time and space.

The structure of ferritin cores has been studied by X-ray diffraction (*47*), electron diffraction (*48*), and high-resolution electron microscopy (*49, 50*). The results indicate that the iron-containing cores of mammalian ferritins are crystalline with a unit cell based on a four-layer

repeat of hexagonally close-packed oxygen atoms with variable octahedral occupancy of Fe(III) ions. The analogous inorganic mineral is ferrihydrite ($5Fe_2O_39H_2O$). Recently, more detailed investigations using HRTEM have been undertaken to determine the structural similarities and differences of individual ferritin cores isolated from vertebrate (human), invertebrate (limpet, *Patella vulgata*), and bacterial (*Pseudomonas aeruginosa*) sources (*50*). Whereas a predominance of single crystalline cores were observed for human ferritin cores, limpet and bacterial ferritins gave very few lattice images. Limpet cores imaged with resolvable lattice fringes contained crystalline domains with dimensions in the range of 30–50 Å. Bacterial ferritin cores, on the other hand, showed only incoherent fringe patterns suggesting lamella-like structures in which the ordering was extremely short range (often 10–20 Å). These differences were also reflected in the different ^{57}Fe Mössbauer spectra obtained from these samples (Fig. 10) (*51*). Human ferritin cores were superparamagnetic (i.e., antiferromagnetically coupled particles of small dimension) with a blocking temperature of ~40 K. Limpet ferritin had a lower blocking temperature (~20 K) and there was also evidence for magnetic disorder. Bacterial ferritins, in contrast, were magnetically disordered down to a temperature of 4 K.

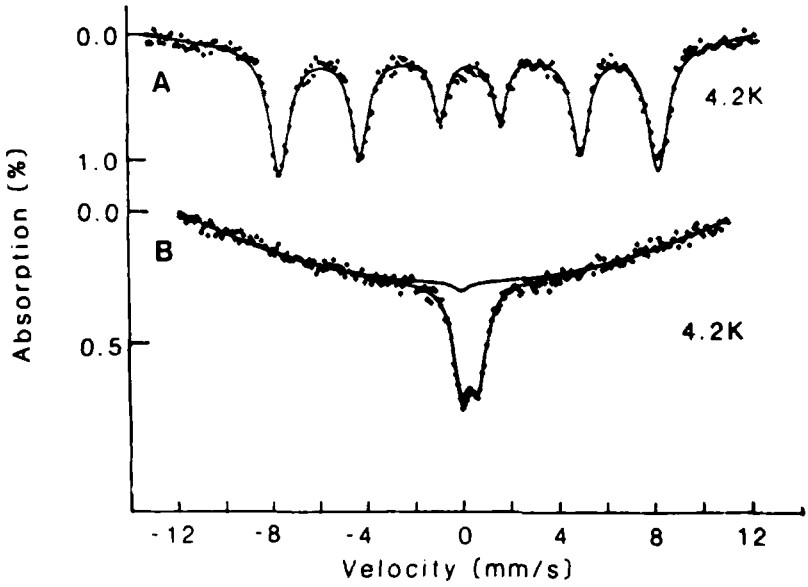

FIG. 10. ^{57}Fe Mössbauer spectra recorded at 4.2 K for (A) human and (B) bacterial ferritin.

These results show unequivocally the fundamental difference in the crystallographic nature of ferritin mineral cores isolated from human, limpet, and bacterial sources. Factors governing this change in crystallochemistry include the rate of oxidation of Fe(II) on entry into the protein cavity and the subsequent mechanisms of growth of the Fe(III) solid phase. These factors will be dependent on local redox and pH conditions, ionic concentrations (influx and efflux rates), and binding sites at the protein interface. For example, rapid oxidation of Fe(II) will kinetically favor amorphous and poorly ordered ferrihydrites. Another factor that may be important is the much higher inorganic phosphate level in the bacterial iron-containing cores. This protein may contain hydrated iron(III) oxyphosphate cores rather than the iron(III) oxide phases of invertebrate and vertebrate proteins.

In order to elucidate the factors that may be important in determining these structural differences, experiments involving the structural and magnetic characterization of reconstituted horse spleen and bacterioferritins have been undertaken (*52*). Reconstitution to an Fe loading of ~3000 atoms was undertaken in the absence of phosphate at pH 7.0 and the cores were compared with those of native proteins. The initial rate of core reconstitution was significantly faster for bacterial (*Azotobacter vinelandii*) compared with horse ferritin. The reconstituted bacterial ferritin cores were pseudocrystalline-defect ferrihydrite compared with the amorphous cores of the native protein. A similar increase in crystallinity was also observed in the reconstitution of *P. aeruginosa* bacterioferritin. These structural modifications imposed by *in vitro* reconstitution suggest that the bacterial proteins do not function primarily as crystallochemically specific interfaces for core mineralization *in vivo*. The absence of phosphate during reconstitution suggests that a major influence determining core structure may lie in differences in cellular physiology that lead to coavailability of Fe and inorganic phosphate in the bacteria and compartmentalization of these components in higher organisms.

C. Group IIA Carbonates and Sulfates

1. Calcium Carbonate

Calcium carbonate minerals are deposited in a wide variety of bacteria, protozoa, algae, higher plants, and invertebrates (Table I). They are also formed, although not as frequently, in vertebrates. The major structural polymorphs identified in biological systems are calcite, aragonite, and vaterite, although there is also evidence for monohydrate, amorphous, and a range of Ca/Mg carbonate phases.

In order to illustrate the structural–chemical features of calcification, two biological systems, namely, calcite and aragonite crystals in inner-ear gravity devices and calcite formation in a marine unicellular alga, *Emiliania huxleyi,* will be reviewed.

a. Calcium Carbonate Mineralization in Gravity Sensors. The inner ears of all vertebrates contain mineral deposits located over specialized sensory areas. These deposits function as detectors of changes in linear acceleration and thus act as gravity sensors. In many organisms, the deposits form as a multitude of minute (~10 μm) crystalline-like structures called otoconia ("ear dust"). In bony fishes, however, the deposits occur as large, single mineral masses called otoliths ("ear stones"). Otoconia of cold-blooded vertebrates consist of aragonite, whereas warm blooded animals form calcite deposits. Otoliths are nearly always aragonitic in structure.

There has been much controversy over the precise crystallochemical nature of inner-ear deposits. Otoliths appear to be polycrystalline deposits (*53*). Otoconia, in contrast, show an evolutionary trend toward small (10 μm), discrete, elongated structures with pseudo three-fold symmetry characteristic of single crystals of calcite extended along the crystallographic *c* axis (Fig. 11) (*54*).

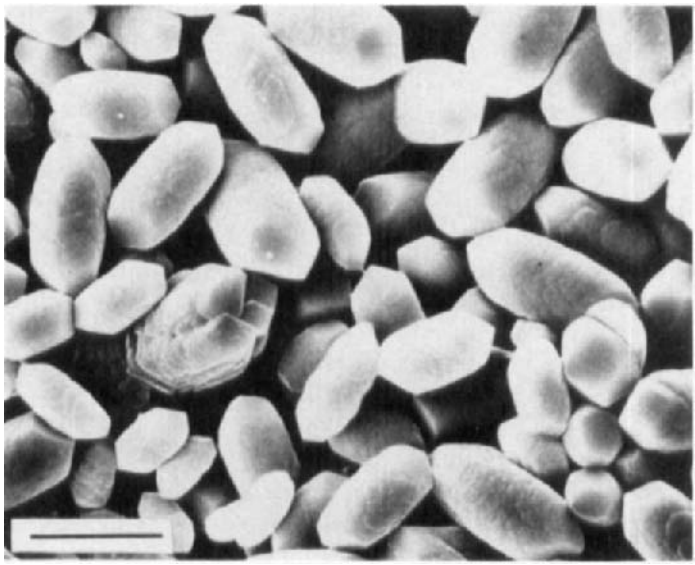

FIG. 11. Calcite rat otoconia. Note the characteristic rounded bodies and crystallographic end faces. Bar = 8 μm.

HRTEM has been used to resolve the degree of three-dimensional perodicity of otoconia and otoliths. Fish otoliths, frog (aragonite), and rat (calcite) otoconia have been studied in detail (*55*). Samples were prepared by crushing to a fine powder in a mortar followed by examination in the electron microscope. Inorganic minerals, treated in the same way, yielded a wide range of crystallites with uneven dimensions and distinct crystallographic edges. In contrast, the crushing of the biogenic minerals resulted in rounded crystallites approximately 0.1 μm in diameter. Electron diffraction patterns generated by the fragments from each sample fell into distinct groups and showed that the biominerals frequently do not expose the same faces as the geological minerals when crushed. Inorganic aragonite was always observed to expose the (010) face whereas the biogenic aragonites gave many faces, including (001). This difference was even more marked in the calcitic minerals. Iceland spar shattered to give exclusively high-index faces, with (221) and (421) especially common. The rat otoconia, however, showed a high predominance of the (001) face.

Fragments from rat otoconia were often platelets with curved edges and were approximately 50–100 nm in size. Lattice imaging and electron diffraction patterns revealed that the platelets were single crystals, although some stacking faults were occasionally observed. These units are the fundamental components from which the bulk otoconia structure is generated. Each single crystallite must undergo controlled nucleation and growth, as shown by the high degree of perfection in the lattice images. The initial nucleation center for each crystallite is possibly at an organic core formed within a cellular vesicle (*56*). The direction and extent of growth are subsequently controlled by the organic material in which the nuclei are embedded. In this way single crystallites are nucleated in vesicles and are continually exocytosed into an extracellular matrix. The organization of this matrix then determines the accretion of the primary crystallites such that the crystallites become oriented along radial lines that fan out until their edges evolve into a continuous bulk crystal face, which is then inhibited from further development. The structural data, therefore, suggest a "multiisooriented" crystalline nature for the otoconia in which the calcite and organic components are in close contact. Although the final structure has the appearance of bulk calcite single crystal, this reflects the degree of spatial ordering of primary crystallites rather than the intrinsic periodicity of a bulk crystalline phase.

Fragments ($\sim$100 nm) of biogenic aragonite from frog otoconia were also shown to be single crystallites by lattice imaging and electron diffraction (*55*). However, unlike the inorganic aragonite fragments,

the biogenic material was unstable under the electron beam. Small areas of amorphous material about 50 Å in diameter were observed within the single crystalline domains. A similar phenomenon was also observed for biogenic aragonite fragments derived from fish otoliths. Under prolonged exposure, the biogenic aragonite electron diffraction patterns showed additional spots, indicating a lowering of crystal symmetry to a primitive lattice. This modification suggests a loss of minor components from the crystal lattice without altering the geometry of the Ca ions. Chemical analysis revealed the presence of Na, Sr, Mg, and P within the native otolith structure. Thus the amorphous regions probably correspond to localized centers of these interstitial ions.

b. Calcium Carbonate Mineralization in Algae. Certain marine unicellular algae, for example *E. huxleyi,* synthesize an elaborate calcitic extracellular shield comprising an intricate network of delicately sculptured oval-shaped calcite plates (coccoliths). The morphology of these plates varies in different species. In *E. huxleyi* the coccoliths are composed of a radially arranged array of crystalline segments, each consisting of a flattened lower element, a hammer-shaped upper element, and a vertical central element (Fig. 12). The vertical element connects the other two regions and forms part of the wall of a central cylinder in each coccolith.

Watabe (*57*) proposed, using electron diffraction, that each radial segment in the coccolith was a single calcite crystal of unique and novel morphology. HRTEM studies (*58*), in contrast, showed that there were different ultrastructural details according to the position of anal-

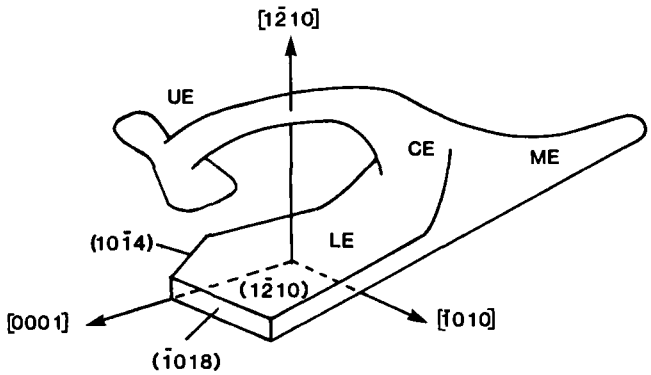

FIG. 12. Drawing showing the crystallography of an individual radial segment of a coccolith of *E. huxleyi.* UE, Upper element; CE, central element; ME, medial element; LE, lower element.

ysis within the radial elements. Lattice images and single-crystal electron diffraction patterns of the basal plate (lower element) were readily obtained due to the thinness of this structure. In contrast, HRTEM images of the irregularly shaped upper elements revealed that these structures were polycrystalline, comprising random arrays of microcrystals often 300–500 Å in size. However, more recent HRTEM studies (*59*) have shown that the whole coccolith element is a highly ordered single crystal. The earlier HRTEM results were from samples possibly damaged by the electron beam of the microscope.

Single-crystal electron diffraction patterns and lattice images were obtained from individual lower elements and from local regions within these segments, and the crystallographic directions in these patterns were correlated with their associated TEM images. Viewed from above the coccolith plate, the diffraction patterns for the lower elements corresponded to the $[1\bar{2}0]$ crystallographic direction (*a* axis) of calcite (Fig. 12), indicating that the top face of the lower element corresponds to the $(1\bar{2}0)$ face of calcite and that the bottom face corresponds to the $(\bar{1}20)$ crystal face. Furthermore, the patterns showed that the crystallographic [001] (*c* axis) direction was oriented parallel to the direction of elongation of the lower element and that the faceted outer edges of each lower element corresponded to the $(\bar{1}08)$ and (104) faces of calcite viewed end-on. Interestingly, the $(\bar{1}08)$ face was always more extensively developed and positioned to the left when viewed from above the base plate (Fig. 12).

Electron diffraction patterns recorded from isolated upper elements showed that these complex units were well-defined single crystals. The *c* axis was oriented parallel to the long axis of the upper element and the hammerhead extension at 90° to the stem corresponded to the [100] direction. The alignments of the crystallographic axes were coincident with those determined on the base plate, indicating that the whole segment was a continuous single crystal.

2. *Strontium and Barium Sulfates*

A range of organisms has been studied in which strontium and barium sulfate are precipitated as crystalline deposits. The studies are of interest in that these two minerals each have one major crystal form, namely, celestite and barite, respectively, with {001}, {011}, and {210} being the principal crystal faces expressed for the geological minerals. However, the biologically produced crystals exhibit many morphologies. The analysis of the morphology of the biogenic crystals yields information about the solution conditions and other controlling factors of crystal nucleation and growth (*60*). Departures from the equilibrium

morphologies produced under crystallographic control indicated that the extent of biological regulation was variable in different organisms.

a. Acantharia. Studies of the crystallography and morphology of the celestite skeleton of the marine protozoan acantharian species *Phyllostaurus siculus* H. (*61*) have provided much information relating to the competition between the requirement of a biological organism to achieve structural functionality and the crystallographic limitations imposed on growth patterns through structural inorganic chemistry. The strontium sulfate skeleton for this organism is built up from 20 spicules radiating from a central point (Fig. 13). The spicules connect via lateral wing structures that are part of the base formations at the innermost end of each spicule. Morphological information obtained from SEM and TEM studies has shown that three types of spicules are present, which can be categorized according to the morphology of the bases and the number and orientation of the lateral wings. The three different spicule types, A, B, and C, were oriented along the crystallographic *a* axis with the lateral wing attachments lying along low-index planes of strontium sulfate (Fig. 14). The spicule bases were observed to join at the center of the cell by the connection of two lateral wings in

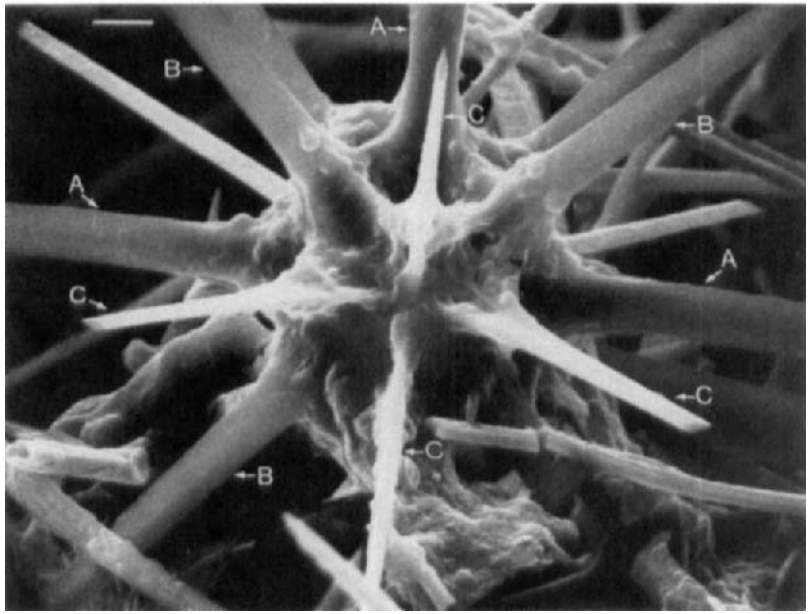

FIG. 13. SEM micrograph showing spicule connectivity within an acantharian. Spicule types are labeled A, B, and C (see Fig. 14). Bar = 5 μm.

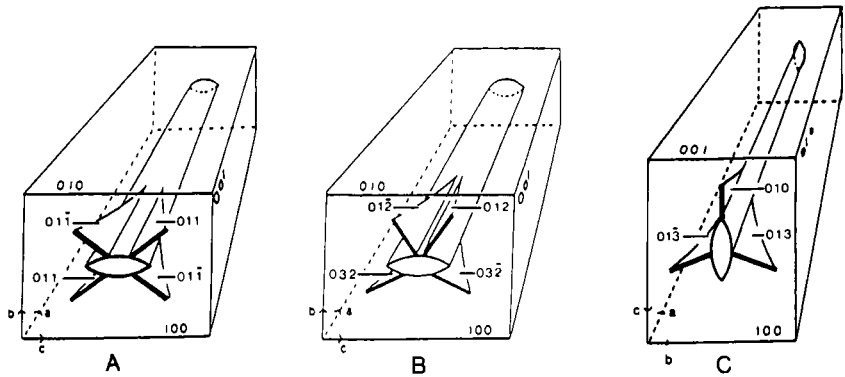

FIG. 14. Schematic representation of the three acantharian spicule types, A, B, and C showing the relation between spicule morphology and crystallographic orientation. The faces of the lateral wings are labeled; a, b, and c refer to the orientation of the unit cell axes of $SrSO_4$ (celestite).

one plane. The pattern of spicule connectivity is such that four type A spicules lie in an equatorial plane and are attached to eight type B spicules, four in a layer above and four in a layer below. The type B spicules are rotated around a central pole, perpendicular to the equatorial plane and by 45° relative to the type A spicules. The type B spicules are also attached to type C spicules, which meet at the poles of the spherical arrangement of spicules. The spicule arrangement is governed by lateral wing attachments lying in low-index preferred planes of strontium sulfate. Examination of the efficiency of spicule packing indicates that the spicule arrangement observed is governed by a compromise between the drive for an efficient use of space at the cell center and crystallographic limitations on lateral wing orientation. The most efficient use of space at the cell center would require all spicules to be identical and to have three lateral wings inclined at 120° to one another. However, this is not compatible with the orthorhombic crystal chemistry of strontium sulfate and is not observed (*61*). The specific and unusual morphology of the spicules and the well-defined relative spicular orientation are indicative of the influence of cellular activity as well as crystallographic considerations in skeletal morphology.

b. Radiolaria. *Sphaerozoum punctatum* is a silica-skeleton, colonial radiolarium found near the ocean surface. During reproduction, the species releases flagellated swarmers containing celestite ($SrSO_4$). These single crystals have an unique morphology based upon an elongated square prism of {011} and possibly {023} faces capped with {210}

triangular end faces (*62*). Crystal surfaces are slightly curved, suggesting membranous involvement or restrictions during growth. A study of the crystals at different states of development has shown that the length of the crystals increases at a far greater rate than the width, suggesting that growth along the principal crystal axis is less constrained. For this system, information on the surrounding membrane structures thought to be involved in the control of crystal development has been obtained by a combination of freeze drying and cleavage of intact samples and by staining and sectioning developing swarmers (*63*). Each crystal is surrounded by an organic membrane that undergoes a series of changes throughout the crystal deposition cycle. Based on observations of crystals of varying sizes, it appears that growth proceeds primarily from one end, resulting in a final crystal that is slightly larger at the base than the tip. This is a mechanism similar to the growth of bullet-shaped bacterial magnetite crystals described in Section II,B,1.

c. Desmids. Desmids are unicellular algae that deposit barium sulfate crystals. In direct contrast to the strontium sulfate deposits in acantharia and radiolaria, wherein specific nonequilibrium biologically controlled morphologies are observed, there appears to be only limited biological control over crystal development in desmids (*64*). The barium sulfate crystals found in these organisms have the same crystallographic faces as those produced by synthetic methods and may exhibit variations on rhombic or hexagonal crystal morphology. Desmids can be grown easily in culture and the extent of biological control on selected ion uptake and mineral formation has been investigated (*64*). Changes in the $Ba^{2+}:SO_4^{2-}$ ratio in the external culture medium resulted in a change in morphology of biogenic crystals (Fig. 15). For $Ba^{2+}:SO_4^{2-} < 1:1$, rhombic crystals were formed, whereas if $Ba^{2+}:SO_4^{2-} \geq 10:1$, hexagonal crystals were observed. If strontium was present in the medium, the organisms readily incorporated strontium into their crystals. Strontium-rich and barium-rich crystals faces were produced in the biological crystals, a phenomenon that is currently being investigated for synthetically produced crystals. The biologically produced crystals had perfect geometries, although, as with synthetically produced crystals, the introduction of Sr^{2+} ions to the system led to the production of more rounded crystals. In general, the morphology of the crystals produced was largely independent of cation identity but was dependent upon the cation : anion ratio in the external growth medium. Further studies have investigated the elemental composition of desmid crystals and have evaluated the extent of biological control over the chemical composition of the

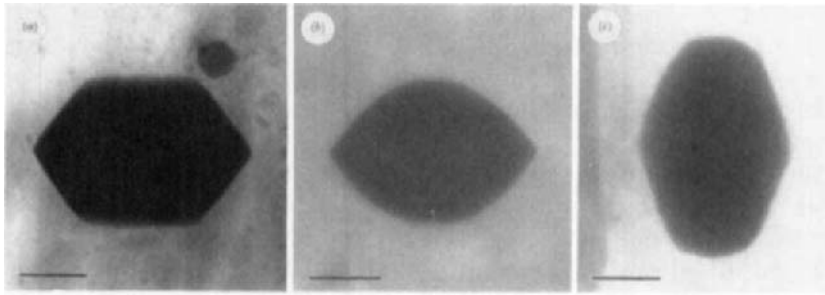

FIG. 15. TEM of tabular crystals from the desmid *M. thomasiana* showing changes in shape on increasing the metal : sulfate ratio in the external environment of a cell culture. Rounded crystals are obtained as strontium substitutes into the barite lattice. Bar = 0.5 μm.

crystalline phase (*65*). The incorporation of isostructural cations (Sr^{2+} and Pb^{2+}) and anions (SeO_4^{2-}, CrO_4^{2-}, and MoO_4^{2-}) into the growth medium resulted only in strontium being incorporated into the crystal phase. Clearly, biological elemental selection against some elements is strong.

3. *Mechanisms of Carbonate/Sulfate Mineralization*

There are several common processes involved in mechanisms of carbonate and sulfate mineralization in unicellular organisms. In both *E. huxleyi* and acantharia, membrane-bound vesicles are used to direct the shape, structure, and crystallographic orientation of the bioinorganic solids. Three key processes are controlled: ionic concentrations (supersaturation), nucleation, and growth.

a. Control of Supersaturation. High levels of intracellular Ca, Sr, and Ba are toxic to cells and hence crystalline deposits are only formed in membrane-bound compartments. These compartments provide localized environments for the chemical control of biomineralization. Ionic concentrations and activities can be regulated and the crystal morphology controlled through the maintenance of specific levels of supersaturation and by the presence of extraneous ions within the surrounding membrane. A clear example of this type of control has been illustrated by studies of $BaSO_4$ crystallization in desmids.

b. Control of Nucleation. The first stage in coccolith biosynthesis in *E. huxleyi* involves the formation of a polysaccharide-rich organic base plate apposed to the nuclear envelope (*66–68*). The nucleation sites for calcification are at the rim of this plate. Crystallites are ini-

tially formed that subsequently grow in lateral, medial, and distal directions to form the complete segments of each coccolith. The precise orientation of crystal nuclei on the surface of the organic base plate indicates that the molecular nature of the underlying organic surface must be of paramount importance. One possibility is that there is a close stereochemical and geometrical correspondence between Ca-binding sites on the organic substrate and lattice sites in the $(\bar{1}20)$ crystal face of the calcite nuclei. It is important to note that it is the $(\bar{1}20)$ face and not the symmetry-related $(1\bar{2}0)$ face that is in direct contact with the organic surface. The nature of the molecular recognition processes active during the nucleation stage is therefore extremely precise.

The Ca atoms coplanar within the $(\bar{1}20)$ face lie in rows parallel to the (104) edge and are separated by distances of 4.03 Å in each row and 6.4 Å between adjacent rows. These spacings must correspond to commensurate configurations of binding sites on the surface of the polysaccharide base plate. The composition of the polysaccharide isolated from the coccoliths of *E. huxleyi* (strain F61) is known and includes at least 13 different monosaccharides, among which uronic acid and methylated and dimethylated sugars are present (*69*). Borman *et al.* (*70*) have shown that the uronic acid moieties interfere with the *in vitro* crystallization of calcium carbonate. It is feasible that Ca binding to the carboxylate groups, as well as to the sulfate residues, could occur in an organized fashion if the polysaccharide molecules of the base plate were ordered. Three major constraints relating to the mode of interaction of Ca atoms and carboxylate groups on the rigid polysaccharide are required for nucleation to occur on the $(\bar{1}20)$ face. First, the O—C—O-binding unit of the ligand must lie approximately perpendicular to the surface of the organic base plate if it is to mimic the stereochemical requirements of carbonate groups in this face; furthermore, the coincidence of the [001] axis and the direction of elongation of the lower elements imply that the O—C—O-binding unit must be also oriented perpendicular to this direction. Second, the arrangement of and distance between Ca binding sites at the interface should match those in the plane of the $(\bar{1}20)$ face, i.e., linear arrays of sites separated by approximately 4 Å within and 6.4 Å between each row. Third, the arrangement of the sites across the interface must be such that the symmetry elements describing this organization are compatible with the deposition of the $(\bar{1}20)$ face and not the $(1\bar{2}0)$ face; this selectivity occurs because these faces are chiral such that the polysaccharide-binding sites can be assembled in a mirror-image configuration specific to the Ca atoms in the $(\bar{1}20)$ face. These criteria could be satisfied, for

example, if linear chains of polysaccharide molecules separated by a distance of approximately 6.4 Å were preferentially aligned at the nucleation site.

These investigations highlight the precise interplay that exists in organisms between the processes of biological organization and the inanimate crystallochemical forces present in inorganic minerals. The matching of specific crystallographic axes with the morphological requirements of biological structures and the tailoring of crystallography in biomineralization must ultimately reflect the evolution of molecular specificity among organic macromolecules and inorganic crystal surfaces. The nature of these interactions has been elucidated through the use of model systems as described in Section III.

c. Control of Growth. The formation of elaborate crystal morphologies can be explained by the shaping of surrounding organic membranes. For example, the outgrowth of each oriented calcite nucleus from the rim of the base plate in *E. huxleyi* takes place under conditions akin to inorganic precipitation, except that the extent of growth is spatially restricted.

The types of external stresses involved in the regulation of crystal morphology are highlighted in the studies of $SrSO_4$ mineralization in acantharia, in which the intracellular vesicles are extended by the cell membranes and filaments that are spatially organized with respect to the developing spicules (Fig. 16). The chemistry of the mineral phase is totally prescribed (there is only one crystalline polymorph of strontium sulfate) and the supply of material is largely a matter of transport, e.g., Sr^{2+} and SO_4^{2-}, and not of metabolism. We note again that the crystal habit is not that observed *in vitro* and the spicule morphology is species specific (*71*). In trying to understand how such a morphology might arise, the competition between crystallochemical and biological controls on morphology must be considered. The argument is presented in detail elsewhere (*72*). Studies of the early growth stages in acantharia (*71*) showed that the cell morphology may be decided quite early in growth if the spicule or filament growth rate is more rapid than the growth rate of the whole cell. The growth of crystals inside vesicles can only continue if the vesicle also continues to grow. If the growth rate of the vesicle and the developing spicular crystal is more rapid than general cell growth, then at an early stage in development the vesicle will hit the cell membrane. Interestingly, the crystal continues to grow with the same habit and it appears that (1) a shape is forced upon the cell and (2) all further development of the system is as an "equilibrium growth" of all components. There must be an interactive balance be-

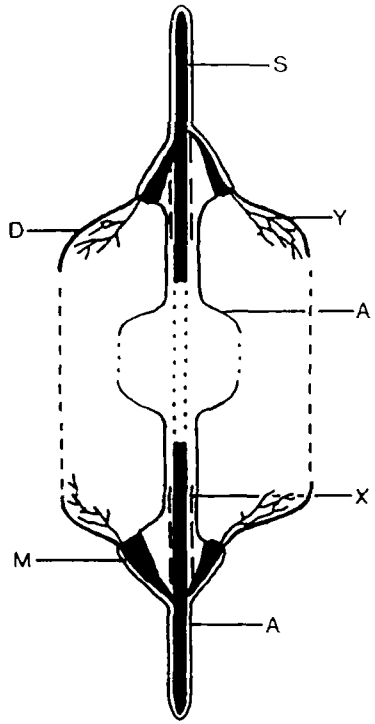

FIG. 16. Schematic diagram showing the effects of cell filaments and membranes on spicule growth in acantharia. S, Spicule enclosed within a vesicle membrane; A, cytoplasmic membrane; D, cortex membrane; Y, cortex filaments; X, tubulin filaments; and M, myoneme (muscular structure).

tween all components if the shape is to be maintained, as growth of one component would result in the development of stress fields for the others, e.g., mineral growth could produce stresses on membrane and filament components or membrane and filament positions may have an effect on crystal morphology. When cell growth, including membranes and filaments, terminates, the shape of the cell could remain fixed, as during the equilibrium growth stage. If the supply of ions, Sr^{2+} and SO_4^{2-}, to the mineralizing site continues, then vesicle and crystal growth would take place in regions of least resistance, i.e., perpendicular to the line of original growth resulting in (1) curved mineral structures under the restraining cortical membrane and muscular myoneme structures or (2) a rectilinear grid of mineral deposited under essentially inorganic conditions.

It may then be that an initial action (the formation of a vesicle with a growing crystal inside it) can generate a morphology without further complex genetic instruction except in the supply of materials. We may suppose that as well as cell shape this morphology includes (1) filament lengths, (2) membrane curvature, and (3) disposition of proteins and other chemicals in the membrane. Thus it is possible that biogenic crystal morphologies can be used to follow the force fields in a single cell.

The relative contributions of physical (including crystallographic) and biological controls over crystalline mineralization processes can vary widely. An interesting comparison with the strontium sulfate acantharian skeleton are the crystals of isostructural barium sulfate found in the vacuoles of desmids. In desmids, filaments and microtubules are absent from the site of mineralization (*73*) and the crystal morphology is similar to that observed in synthetic systems. The level of biological control is minimal and the crystal form appears to be principally controlled by inorganic physical crystallochemical stresses. The barium sulfate crystals so formed bear no morphological relationship to the cell in which they grow. This substantiates the idea that filaments and microtubules must play a major role in determining mineral morphology in species such as acantharia.

D. Composite Biominerals; Limpet Teeth

Biominerals are composite phases constructed from a variety of inorganic and organic components for which the roles of molecular (both inorganic and organic) species in the control of biomineral growth, morphology, and composition are being increasingly recognized. Several organisms contain mineralized structures containing a complex arrangement of several minerals. Examples include limpet and chiton teeth and stinging hairs from the common stinging nettle. The compositional complexity of such materials makes the characterization of biominerals particularly challenging. It is important to identify the components present and to obtain information on the biological environment in which synthesis takes place. This information can only be obtained using a range of structural and analytical techniques, including electron microscopy (SEM, TEM, HRTEM, and electron diffraction), X-ray microanalysis (EDXA and SPM), and a range of molecular spectroscopies, including Mössbauer spectroscopy (^{57}Fe) and solid-state NMR spectroscopy (^{29}Si). In this section we review the compositional and structural chemistry of iron oxide and siliceous minerals found in

limpet teeth and give some indication of the interrelationship between the different biomineralization pathways.

Limpets are intertidal and shallow-water molluscs that graze on rock-encrusting organisms such as algae and sponges using a specially developed tongue, or radula. The impregnation of the teeth with biominerals [goethite (α-FeOOH) (*74*) and silica (*75*)] enables the animals to excavate to a limited extent the rocks over which they browse. Because the teeth are progressively mineralized along the radula and are continually replaced as the mature teeth are lost by mechanical wear, the radula represents a well-defined spatial and temporal sequence of mineralization that can be mapped structurally and analytically within a single biological specimen.

The changes in elemental composition within intact lateral teeth have been studied by electron microprobe analysis (*76*) and scanning proton microprobe analysis (*77, 78*). The immature teeth are white, unmineralized organic structures and SPM studies show little evidence of any organized distribution of elements, although Fe and Si could be readily detected. SPM elemental maps of the early mineralized teeth (faint brown coloration) indicated that mineralization was initiated within the bases of the teeth, with preferential localization of Fe and P below the junction with the cusp. Elemental concentrations in the cusp of the teeth at this stage were much lower with Fe localized at the posterior side and Si and Ca at the anterior side of the cusp (Fig. 17). As mineralization progressed, the cusp became heavily impregnated with Fe and Si. Fe levels in the cusp were comparable to those in the upper basal region whereas Si levels were approximately constant throughout the teeth. P levels remained high and localized just below the cusp/base junction. In fully mature teeth, distinct boundaries between the major elements (Fe and Si) were observed (Fig. 17) and localized concentrations of Cu were also detected within the cusp. It is important to notice that the distribution of each element follows a particular temporal and spatial pattern.

The elemental distributions determined by SPM mapping indicate the complex compositional changes that occur during the biomineralization of the limpet teeth. In particular, the results identify the developments of the Fe and Si deposits and the presence of other elements that may be of significance in the regulation of biomineralization. For example, the localization of Cu in mature tooth cusps suggests that Cu oxidases have been transported into the tooth to catalyze oxidative cross-linking of phenolic-type material identified by histochemical studies (*79*). The organic material presumably remains flexible until

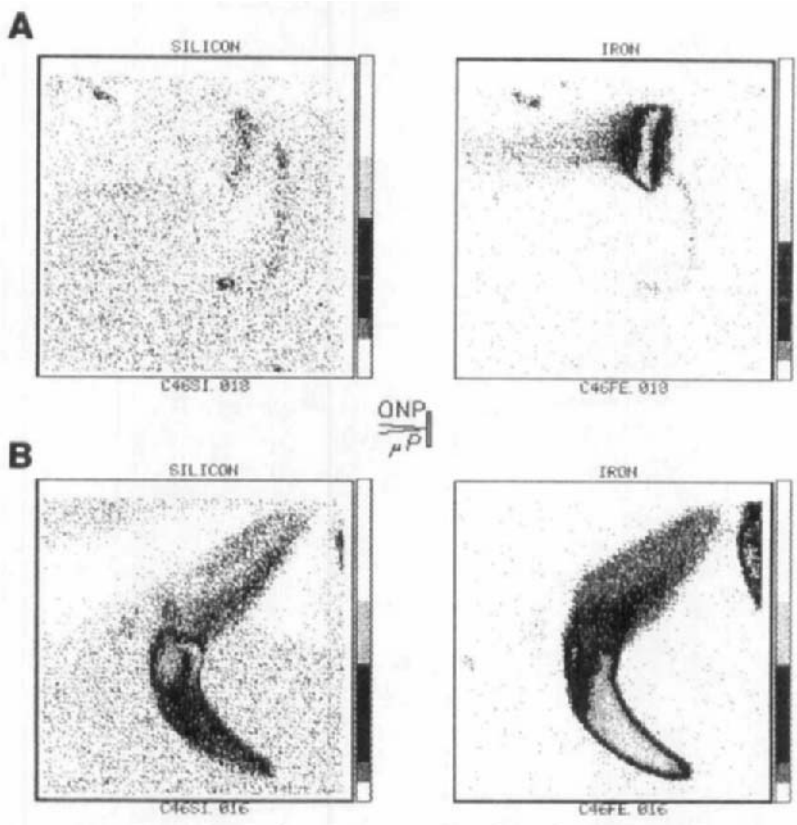

FIG. 17. SPM elemental maps of iron and silicon in (A) immature and (B) mature limpet teeth. The scan area was 200 × 200 μm. The highest concentrations are represented by the lightest grey shading.

much of the inorganic matrix of crystalline goethite and amorphous silica impregnates the tooth.

The structure, morphology, and organization of mineralogical components located within the changing chemical environments identified by SPM studies have been investigated by electron microscopy, electron diffraction and EDXA (*80*), solid-state NMR spectroscopy (*13*), and HRTEM and Mössbauer spectroscopy (*81*).

^{57}Fe Mössbauer spectra of the mature teeth (Fig. 18) showed two components with different magnetic hyperfine field splitting values. Whereas the major component gave six-line magnetically split spectra characteristic of stoichiometric goethite (α-FeOOH) at all tempera-

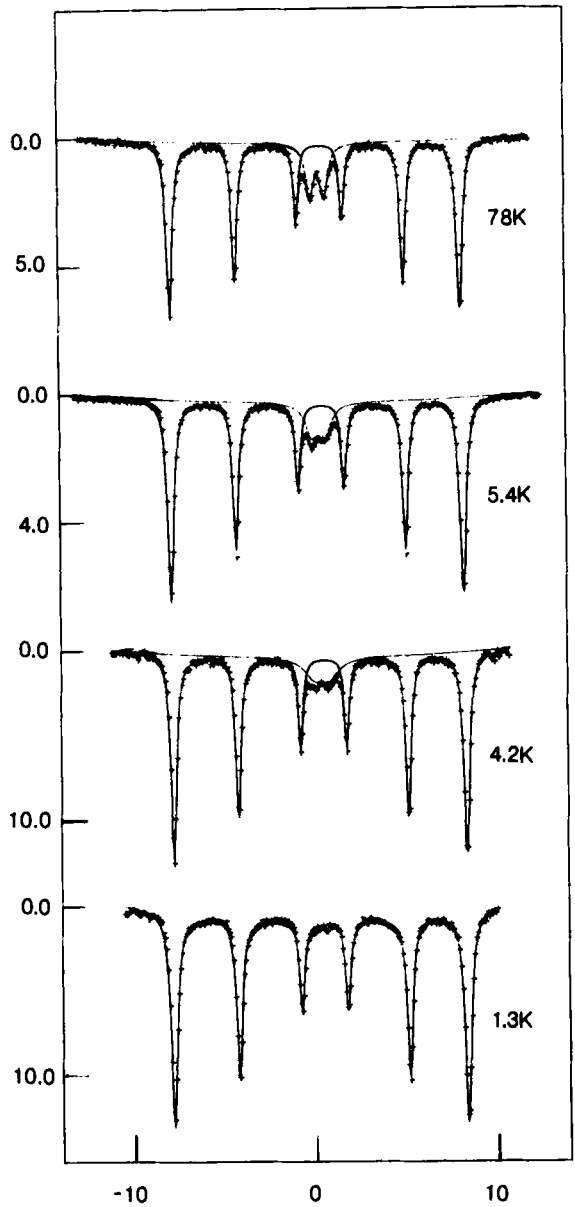

FIG. 18. Temperature-dependent ^{57}Fe Mössbauer spectra of mature limpet teeth.

tures below 400 K, the minor phase (15%) was superparamagnetic, showing a fully saturated quadrupole doublet above 40 K. Spectra obtained from separated bases and cusps of individual teeth confirmed that the goethite was located primarily within the cusps and that the bases contained the superparamagnetic material.

Electron microscopy studies showed that the tooth cusps were impregnated with stoichiometric well-ordered single crystals of goethite that exhibited characteristic acicular morphology. Sectioned teeth showed the remarkable degree of organization of these crystals within the tooth cusp. Crystals at the posterior and anterior edges were oriented approximately parallel to the long axis of the tooth, whereas those in the center of the cusp were interwoven in three dimensions. The mineral components of the tooth base were of mixed composition and showed a variety of structural forms. Irregular lathes of goethite with growth inhibition in the [001] direction, microcrystalline granular material comprising both 5-nm irregular domains of goethite and material rich in Si and Fe (trace Ca), sheetlike material high in Ca and P with trace Fe and Si, and particulate material of variable composition (Si, Fe, Ca, P, Cl, and Zn in decreasing concentration) were all detected.

HRTEM was used to investigate crystal growth in the tooth cusps. The crystals were deposited in the form of thin fibrous strands (15–20 nm in width) adjacent to underlying organic filaments (Fig. 19). Crys-

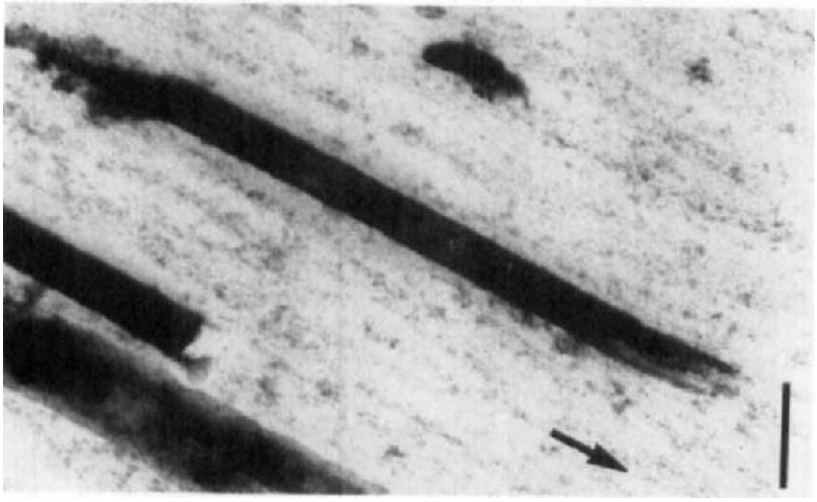

FIG. 19. High-magnification image of an aligned goethite crystal and stained organic fibrous material running parallel to the crystal growth direction (arrow). Bar = 0.1 μm.

tal growth occurred primarily by increases in width such that the mature acicular crystals were aligned with the [001] crystallographic axis parallel to the organic substrate. Spatial deviations in the filaments were reflected in marked growth distortions in some of the mature crystals. Lattice imaging of the immature fibrous crystals revealed the presence of lattice discontinuities, ill-defined crystal edges, and mosaic patterns indicating extensive irregularities in crystal thickness and structure. Thus the early stage of crystal growth appears to be somewhat discontinuous, suggesting fluctuating rates of Fe(II) transport to the mineralization sites from the surrounding epithelial cells.

Removal of iron from mature teeth by acid treatment resulted in silica-impregnated cusps of marked structural integrity. Blocks of silicifed material were found at the junction zone between the cusp and tooth base. The outer surfaces of the teeth were generally smooth and showed little evidence of etch pits due to the removal of iron-containing minerals. However, fractured teeth indicated the presence of localized silica-rich anterior zones within the tooth cusps.

Silica deposition within the interior of the cusps often showed directional character, with fibrillar elements preferentially oriented both transverse and longitudinal to the axis of the teeth. Some central regions of the cusp comprised random aggregates of fibrillar silicified material. Most internal regions investigated appeared highly porous with extensive voids.

Fracturing of acid treated teeth revealed a range of silicified structures, including globular, sheetlike, fibrillar, and tubular motifs. All the structures were built up from amorphous silica particles 5–15 nm in diameter. Globular material (aggregates, 30–50 nm in diameter) was either disorganized or aligned with fibrillar microstructures (80–180 nm wide) in which the silica phase appeared to impregnate an underlying (organic?) framework often with characteristic helical decoration. Related structures included thin sheets of silica-impregnated material, extensively folded or tubular in morphology (Fig. 20). The elaboration of these substrates with primary silica spheres varied in degree. Tube diameters were generally 30–60 nm, but larger diameters (up to 300 nm) were also observed. The thickened edges of the tubes varied greatly in dimension (12–100 nm) depending on the diameter of the tube and the degree of silica impregnation. Silica particles often showed orientational order within these components. Significantly, many of the silicified hollow tubes had diameters similar to the widths of the goethite crystals, suggesting that iron oxide mineralization occurs within the organic silica-strengthened tubular structures,

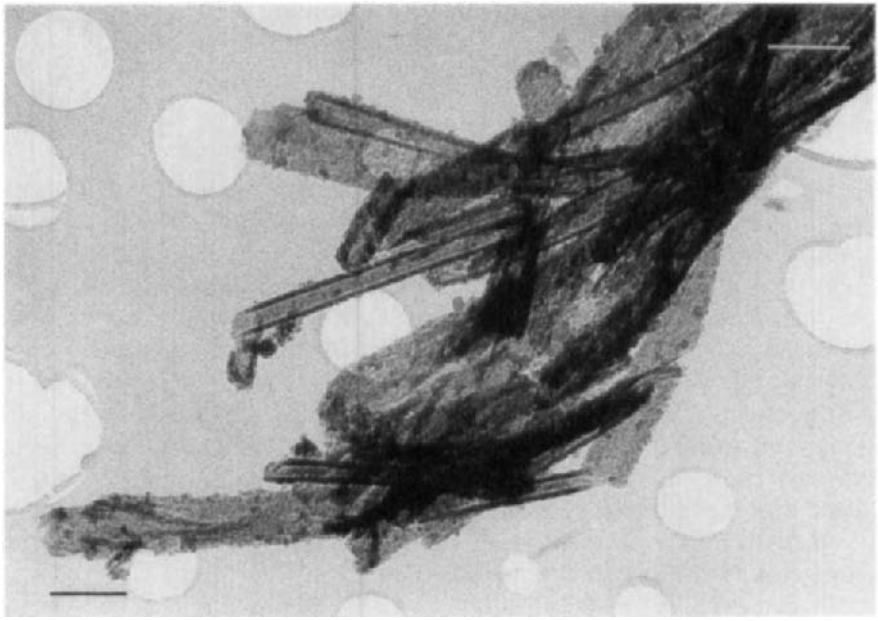

FIG. 20. Crushed fragments of acid-treated limpet teeth showing silicified tubular structures with thickened edges. Bar = 166 nm.

which are subsequently impregnated with additional amorphous silica. Thus silica plays a critical role in the structural integrity of the tooth because the mineral infiltrates space not occupied by the goethite phase and also impregnates, and therefore hardens, the organic matrix components. The ability of silicic acid to bind strongly to catechol-type molecules will enhance this structural function.

Both the SPM and HRTEM results provide a working hypothesis for the crystal growth mechanisms involved in the biomineralization of iron oxides in limpet teeth. The growth of crystals is markedly influenced by the chemical environment of the mineralization zone. Crystals formed in the base are disordered and microcrystalline due to the presence of significant levels of other elements (P, Si, and Ca), whereas the high perfection of cusp crystals is reflected in the greater regulation over the spatial differentiation of all elements transported into the cusp from the surrounding epithelial cells. Growth of crystals in the cusp is slow and regulated by the presence of organic filaments that orientate the crystals along preferred directions depending on their location within the tooth. These observations highlight the role played

by the local structural and chemical environments of biological tissues in the regulation of bioinorganic solid-state reactions.

III. Model Systems

A direct consequence of our biological studies has been the development of chemical model systems for the investigation of crystal or aggregate formation under controlled experimental conditions. Examples presented in this article are taken from our studies of membrane-bound (vesicular) precipitation, solution precipitation and crystallization, and the effect of ordered organic substrates (Langmuir monolayers and multilayers) on nucleation and crystal growth. In all cases the materials formed are compared with phases prepared in the absence of vesicles/additives/substrates in order to assess the role of these factors on various aspects of inorganic precipitation. We anticipate that a combination of biological and chemical model studies will lead to an improved understanding of both biomineralization and the design of new inorganic materials.

A. Phospholipid Vesicles

Many of the above examples of biomineralization have highlighted the central importance of intracellular vesicles in controlling the nucleation and growth of inorganic solids in biological systems. An early objective of our work was to model these processes through the study of precipitation within synthetic phospholipid vesicles of diameter ~30 nm. Our aim was to investigate the types of precipitate that could be formed in confined environments and determine the level of control exerted by these chemically well-defined supramolecular assemblies. For example, the chemistry of formation of intravesicular materials may be very different from the corresponding bulk solution reactions normally encountered in inorganic chemistry. In particular, the chemical and electrical fields generated within the microvolume may be responsible for changes in redox, kinetic, and structural behavior.

Unilamellar phosphatidylcholine vesicles can be readily prepared by sonicating dispersions of the lipid in aqueous solution at a temperature above the gel–liquid transition point. When formed in the presence of metal ions, the internal space contains encapsulated species that can subsequently undergo crystallization reactions with membrane-permeable species such as OH^- and H_2S (Fig. 21). Alternatively, coreactants can be transported into the interior of the vesicles via ionophores sited in the lipid bilayer. The following materials have been investi-

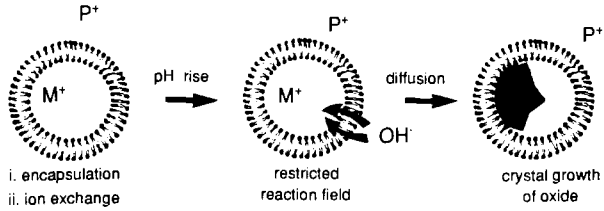

FIG. 21. Reaction scheme for the membrane-mediated crystal growth of metal oxides in phospholipid vesicles.

gated: Ag_2O (*82, 83*), AgS and AgI (*9*), CoS (*2*), $CoSiO_3$ (*84*), Ca phosphates (*85*), $Fe_2O_3 \cdot nH_2O$ and Fe_3O_4 (*86, 87*), Al_2O_3 (*88*), $BaHPO_4$ and SiO_2 (*89*), and $CaCO_3$ (*90*).

Before reaction, encapsulated cations such as Fe(II), Fe(III), and Co(II) bind strongly to the headgroup phosphates of the phospholipid bilayer (Fig. 22A) so that nucleation is localized at the organic surface. Reaction with OH^- resulted in finely divided intravesicular particles (Fig. 22B). Electron diffraction patterns arising from the particles obtained from Fe(III) solutions had *d* spacings corresponding to poorly ordered goethite (α-FeOOH), whereas similar reactions with entrapped $Fe(II)_{aq}$ and $Fe(II)_{aq}/Fe(III)_{aq}$ solutions gave intravesicular particles of spherulite magnetite (Fe_3O_4) and ferrihydrite ($Fe_2O_3 \cdot nH_2O$), respectively. These products were different from those formed under identical starting conditions in the absence of vesicles. For example, precipitation of Fe(III) solutions resulted in extended aggregates of ferrihydrite, Fe(II) solutions gave acicular needles of lepidocrocite (γ-FeOOH) and goethite, and Fe(II)/Fe(III) solutions gave irregularly shaped 10- to 50-nm magnetite particles. Thus there are distinct modifications in structure, morphology, and particle size for precipitation reactions undertaken within unilamellar vesicles. These differences can be attributed primarily to the kinetic control exerted by the vesicle membrane on the rate of OH^- diffusion into the intravesicular space, although the charged organic surface may be important in stabilizing the accumulation of ionic charge and in subsequent formation of the embryonic crystallites.

The transfer of cations across the lipid bilayer and the subsequent intravesicular deposition of $CaCO_3$, $BaHPO_4$, and SiO_2 have been studied. Incorporation of silicate species at pH 10 followed by transport of protons using lasolacid A as an ionophore gave 6- to 7-nm silica particles clustered at the membrane surface (Fig. 23). Reaction times of 2 hr gave dense vesicular precipitates. A similar effect was observed when ionophores such as 18-crown-6 were used to transport Ba^{2+} ions

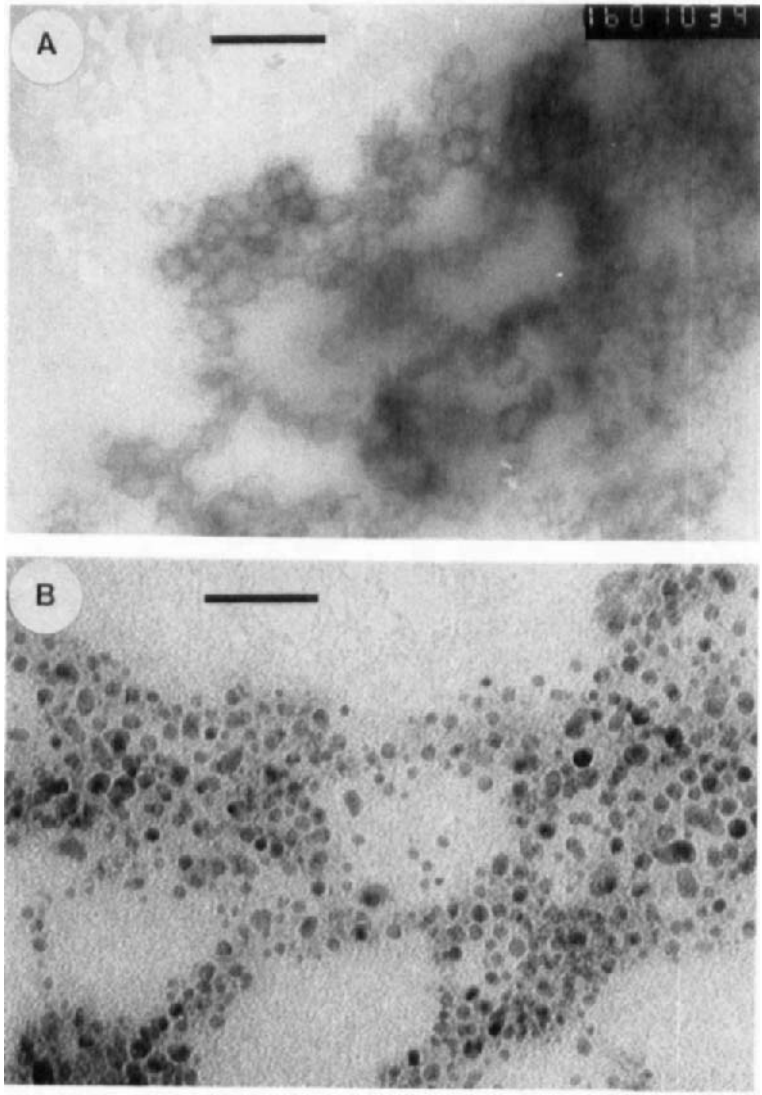

FIG. 22. (A) Transmission electron micrograph showing phosphatidylcholine vesicles containing intravesicular Fe(III) ions at pH 2.0. Bar = 75 nm. (B) Electron micrograph showing discrete intravesicular precipitates 30 min after the addition of NaOH to Fe(III)-containing vesicles. The particles were identified as poorly ordered goethite (α-FeOOH) by electron diffraction. Bar = 30 nm.

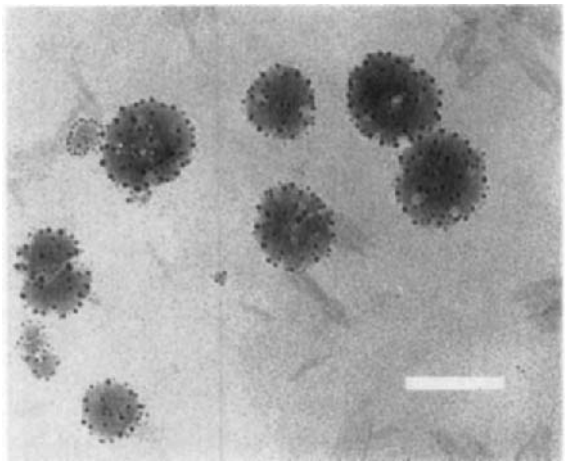

FIG. 23. Transmission electron micrograph showing silica particles associated with phospholipid vesicles. Bar = 100 nm.

into phosphate-containing vesicles. The resulting $BaHPO_4$ crystals were formed around the membrane surface. By contrast, the intravesicular precipitation of Ag_2O from encapsulated Ag(I) solutions that were reacted with hydroxide ions gave discrete crystals of cubic Ag_2O. The formation of intravesicular single crystallites indicates that nucleation proceeds at a single site on the vesicle membrane, compared with the ionophore experiments in which clusters of particles were observed, suggesting that nucleation can occur simultaneously at many headgroup sites.

The kinetics of intravesicular precipitation have been studied by light scattering (*83*). There was a linear relationship between the initial rate of precipitation and trapped Ag(I) concentration at constant hydroxide ion concentrations. Thus, over the concentration range investigated, the initial kinetics were first order with respect to the intravesicular Ag(I) concentration ($[Ag]_{in}$). The dependency on extravesicular pH ($[OH^-]_{out}$) was more complex; at pH values less than 10 no changes in turbidity were observed, at pH 11–12.0 the reaction was strongly dependent on $[OH^-]_{out}$, and above pH 12 the initial rate was essentially independent of $[OH^-]_{out}$.

These data suggest a two-step reaction mechanism for intravesicular Ag_2O precipitation:

$$OH^-(aq)_{out} \xrightarrow{k_{diff}} OH^-(aq)_{in}$$

$$2OH^-(aq)_{in} + 2Ag^+(aq)_{in} \xrightarrow{k} Ag_2O(s)_{in} + H_2O$$

The first step is diffusion controlled and depends on the rate of passage of OH^- ions through the lipid membrane. At pH_{out} values below 11.0, the rate of OH^- influx is very small and supersaturation is never attained within the vesicles. At pH_{out} values above 12.0, the rate of crystal growth becomes less dependent on initial pH gradients across the membrane because the limiting rate of diffusion through the membrane is attained.

The relationship between the intra- and extravesicular pH in the above experiments has been studied by ^{31}P NMR spectroscopy (*91*). Vesicles containing a mixture of NaH_2PO_4 and $NaNO_3$ were studied to determine whether the presence of the diffusable NO_3^- ion would permit the influx of hydroxide as observed for intravesicular Ag_2O formation. The intravesicular phosphate resonance, initially at −14.98 ppm, did not shift significantly until above pH_{out} 11.0, after which it shifted steadily downfield due to OH^- influx (Fig. 23). Similar experiments undertaken with phosphate in the absence of nitrate showed that a pH gradient of ~6 units could be maintained across the bilayer membrane at an external pH of 12.5 (Fig. 24).

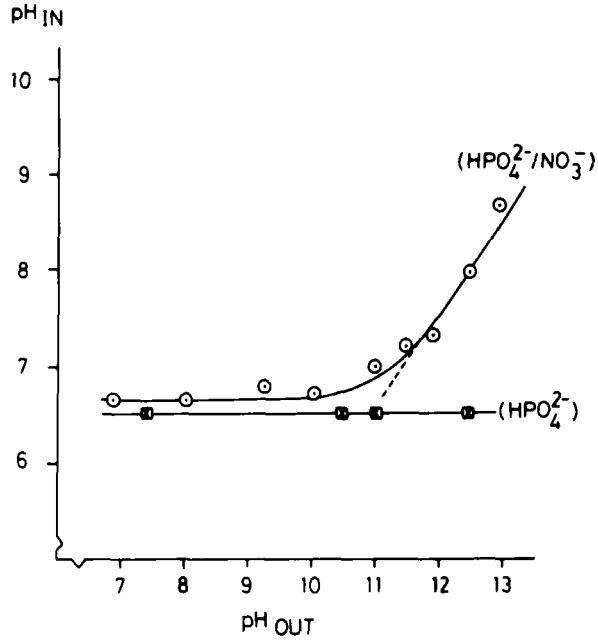

FIG. 24. Plot of intravesicular pH against extravesicular pH for vesicles containing phosphate, with and without intravesicular nitrate; pH values were determined from ^{31}P NMR chemical shifts.

The reduction of the pH gradients across the vesicle membranes in these experiments requires the net transport of OH^- ions into the vesicles. In order to preserve electroneutrality this can only occur if there is an equivalent net migration of anions out of the vesicles. In the experiments with vesicles containing NO_3^-, the internal pH responded to a change in pH_{out} above 11.0, whereas the vesicles containing only the more highly charged HPO_4^{2-} and PO_4^{3-} ions showed no changed in internal pH. Thus the presence of encapsulated diffusible anions is important in determining the role played by the membrane in controlling intravesicular pH, and hence the rate of inorganic oxide precipitation within the internal cavity of the vesicles.

The dependency of the rate at which supersaturation is maintained within the vesicles on anion diffusion rates is clearly revealed when anions of different permeabilities are substituted for OH^- and the corresponding intravesicular precipitation is followed by turbidity measurements (*83*). In the case of intravesicular AgCl formation, the increase in turbidity with time due to the addition of Cl^- was much slower than for Ag_2O formation, indicating that diffusion of Cl^- across the lipid membrane was reduced compared with OH^-. The formation of intravesicular Ag_2S, on the other hand, occurred instantaneously after the addition of $(NH_4)_2S$ due to diffusion of free molecular H_2S across the vesicle membrane.

B. Synthetic Studies

The synthesis of molecular precursors responsible for tailored nucleation and growth is a key feature in the chemical control of biomineralization. Here we highlight recent studies using simplified model systems that aim to identify aspects of solution chemistry important in (1) silica polymerization and aggregation and (2) the morphological design of calcite crystals.

1. Silica Polymerization and Aggregation

A serious problem in the control of silica polymerization is that, in general, initial particle formation is a result of random bond formation between a range of polysilicate species in solution. Moreover, the aggregation process is uncontrolled under conventional preparation conditions. It is important to understand the basic mechanisms of particle formation and aggregation in aqueous solution, as the physical properties of such silicas are determined primarily by the coordination number and nature and strength of interactions between essentially spherical primary particles.

In principle, the use of monomeric soluble silicon species should guarantee a common building block for further polymerization events. In addition, silicon complexes have been implicated in silicon transport in biological systems, enabling a much higher concentration of soluble silicon species to be established than would be possible for monomeric silicic acid alone. We have used six-coordinate silicon catecholate complexes in aqueous or buffered media (pH $\approx$ 7) to study silica polymerization and aggregation phenomena. Initial NMR spectroscopy studies on solutions of ammonium salts of silicon catecholate species showed that at pH 7.0, a 4 m*M* solution of the complex decomposed in about 20 min. At pH 7.4, exchange reactions between different catecholate ligands could be followed. The nature of the buffer had a significant effect on these reactions. Significantly, decreasing water concentrations in the reaction volume led to increased control over the polymerization process. The nature of the precipitates formed varied markedly with pH. For samples prepared from an aqueous environment at pH 6–5, deposits were ill formed and showed extensive necking between 10-nm diameter particles. At pH 7–2, sheetlike deposits were obtained and exhibited minimal interparticulate contact (Fig. 25).

2. Morphological Design of Calcite Crystals

The importance of understanding the mechanisms of controlled morphology in biomineralization has resulted in several synthetic studies aimed at modeling these processes. *In vitro* studies of calcium carbonate crystallization in the presence of macromolecules isolated from mollusk shells indicated that these molecules have a marked inhibitory function (*92*). Recently, Berman *et al.* (*93*) showed that specific morphological changes can be induced in calcite crystals grown in the presence of soluble proteins isolated from the calcified test of the adult sea urchin. The crystals exhibited well-defined faces of $(1\bar{1}0)$ form, suggesting that carboxylate residues of the protein stabilize these faces via selective stereochemical binding.

The biological macromolecules used in these experiments were invariably complex. An alternative approach has been to investigate low-molecular-weight analogs that can be systematically modified in their molecular structure and stereochemistry. Calcite crystals grown in aqueous solutions containing variable levels of functionalized and nonfunctionalized α,ω-dicarboxylates have been studied (*94*). Crystals formed in the presence of malonate were spindle shaped at a mole ratio of Ca : malonate = 3. The crystals were elongated along the *c* axis and exhibited curved $\{1\bar{1}0\}$ prismatic faces. Significantly, these crystals were very similar to the calcite crystals deposited in the inner-ear

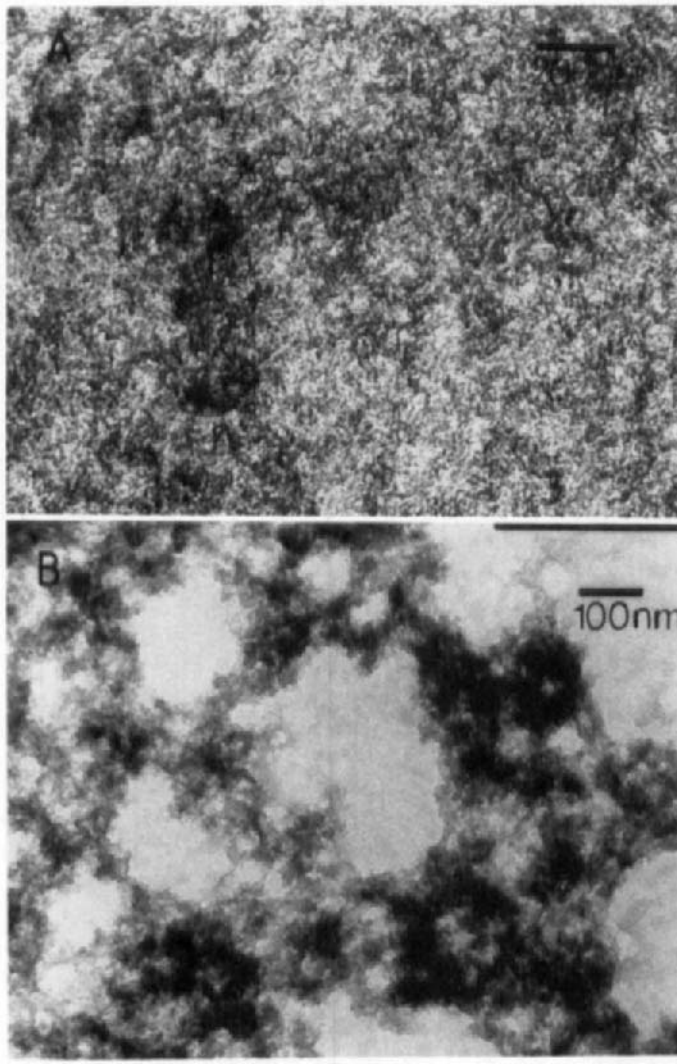

FIG. 25. TEM micrographs of silicas produced from the hydrolysis of silicon catecholate species in aqueous media; (A) pH 7.2; bar = 200 nm; (B) pH 6.5, extensive necking of particles; bar = 100 nm.

gravity devices of mammals and reptiles described in Section II,C,1,a (Fig. 11). The biological crystals are formed in the presence of acidic organic molecules, including proteins containing the malonate residue of the specialized amino acid, γ-carboxyglutamic acid (*95*), suggesting

that these functional groups are responsible for the characteristic shape of the biogenic deposits.

The formation of spindle-shaped crystals was reduced with increasing chain length between the α,ω-carboxylates. The unsaturated derivative, maleate, was also less potent compared with the saturated malonate compound, whereas the trans isomer, fumarate, had minimal morphological effect. Functionalization of the lower chain acids had a marked influence on crystal morphology. Crystals grown in the presence of aspartate (α-aminosuccinate) exhibited well-defined $\{1\bar{1}0\}$ prismatic faces at Ca : additive = 17, whereas γ-carboxyglutamate had a pronounced effect at ratios as high as 85.

The affinity of dicarboxylate molecules for the prismatic faces can be attributed to electrostatic, geometric, and stereochemical recognition at the crystal–additive interface. Incorporation of carbonate into these faces is via bidentate binding to Ca atoms and this can be closely simulated by dicarboxylate interactions, provided that the spacing between carboxylates is close to 4.0 Å. Both malonate and maleic fit this criterion, but the increased rigidity of the latter reduces the binding affinity. The marked effect observed on substitution of an α-hydrogen of succinate for NH_3^+ of aspartate suggests that the amine moiety may be able to substitute for a Ca site cooperatively with carboxylate binding via an extended molecular conformation across several layers of the $(1\bar{1}0)$ crystal surface (Fig. 26). A similar effect, but involving an additional carboxylate, is possible for γ-carboxyglutamate binding.

C. Organized Organic Substrates

One of the most important aspects of biomineralization with respect to crystal chemistry lies in the growing awareness of the potential of organic surfaces to mediate inorganic crystallization. A number of different experimental strategies have been developed to elucidate the mechanisms of inorganic crystallization at organized organic templates. A biological approach has been to isolate the matrix components of mineralized tissue such as bones, teeth, and shells, and to examine the formation of insoluble Ca salts in the presence of these macromolecules. Earlier studies on mollusk shells highlighted the potential importance of epitaxial matching between Ca–Ca distances in the aragonite (001) crystal face and repeat distances of carboxylate functional groups on an antiparallel β-pleated sheet protein backbone (*96*). Later work, using extracted proteins adsorbed onto glass substrates, suggested that stereochemical and electrostatic factors were important (*97*). The difficulty with these studies is that the details of

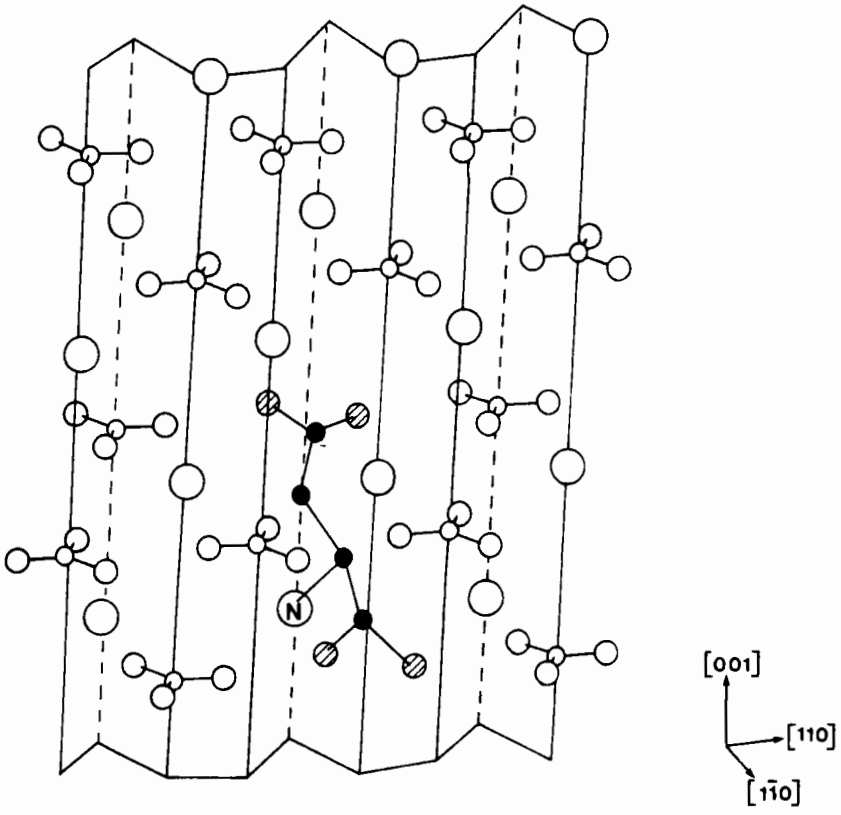

FIG. 26. Perspective drawing of (1$\bar{1}$0) face of calcite showing possible asparate-binding site. Both carboxylate and amine residues can be accommodated at carbonate and Ca sites, respectively. Large open circles, Ca; hatched small circles, carboxylate oxygens; small black circles, C atoms of additive molecule.

the surface structure cannot be assessed because of the complexity of the macromolecules used. Furthermore, *in vitro* conformation of such molecules may be very different from their *in vivo* counterparts.

Recent studies have adopted an approach using simplified organized surfaces that can be characterized and systematically modified. The method involves the use of compressed monomolecular surfactant films formed at air/water interfaces in a Langmuir trough as substrates for inorganic crystallization from supersaturated subphases. Landau *et al.* (*98, 99*) showed that monolayer films of compressed resolved amino acid monolayers could act as templates for the nucleation of inorganic and chiral organic crystals. This approach has been recently extended to the study of $CaCO_3$ crystallization under neutral and charged

Langmuir monolayers (*100–102*) and $SrSO_4$ crystallization (*103*) on hydrophobic and hydrophilic Langmuir–Blodgett films.

1. Langmuir Monolayers

Crystals of $CaCO_3$ were grown from supersaturated calcium bicarbonate solutions (pH 6.0) freshly prepared by purging suspensions of calcite with CO_2 gas for 1 hr. The control experiments gave randomly dispersed aggregates of nonoriented rhombohedral calcite crystals at the air/water interface. In contrast, when compressed monomolecular films of stearic acid $[CH_3(CH_2)_{16}COOH]$ or octadecylamine $[CH_3(CH_2)_{17}NH_2]$ were spread at the air/water interface, the crystals were discrete and crystallographically oriented. For stearic acid at total [Ca] = 10 m*M*, rhombohedral calcite plates were deposited aligned with the $[1\bar{1}0]$ direction perpendicular to the organic surface (Fig. 27A). At a lower concentration ([Ca] = 5 m*M*), a marked structural modification was observed, with the metastable polymorph, vaterite, being exclusively nucleated. These crystals were oriented with the *c* axis perpendicular to the monolayer. In comparison, oriented crystals grown under compressed octadecylamine films were exclusively vaterite, independent of Ca concentration. Moreover, two distinct orientations of these crystals were observed (Fig. 27B). One type was morphologically and crystallographically equivalent to the vaterite crystals formed under stearic acid films, whereas the other type was unique to the octadecylamine monolayers and oriented with the *a* axis perpendicular to the monolayer surface.

These results indicate that both negatively and positively charged compressed monolayers can induce the oriented nucleation of $CaCO_3$ crystals. Significantly, $CaCO_3$ crystallization under neutral octadecanol $[CH_3(CH_2)_{17}OH]$ monolayers was severely inhibited, and under compressed cholesterol ($C_{27}H_{45}OH$) films it was no different from the control experiments. This suggests that ion charge accumulation at the ionized headgroups is a critical factor in regulating crystallization at the organic surface.

The presence of both oriented vaterite and calcite crystals on charged monolayers indicates that the electrostatic interactions between nuclei and the organic surface are influenced by structural relationships at the interface. The nucleation of vaterite on films of positive and negative charge indicates that Ca binding is not a prerequisite for stabilization of this metastable phase. Oriented calcite, on the other hand, requires Ca binding at the carboxylate headgroups.

Nucleation of calcite on the $(1\bar{1}0)$ face under stearate monolayers can be rationalized in terms of charge, stereochemical and geometric com-

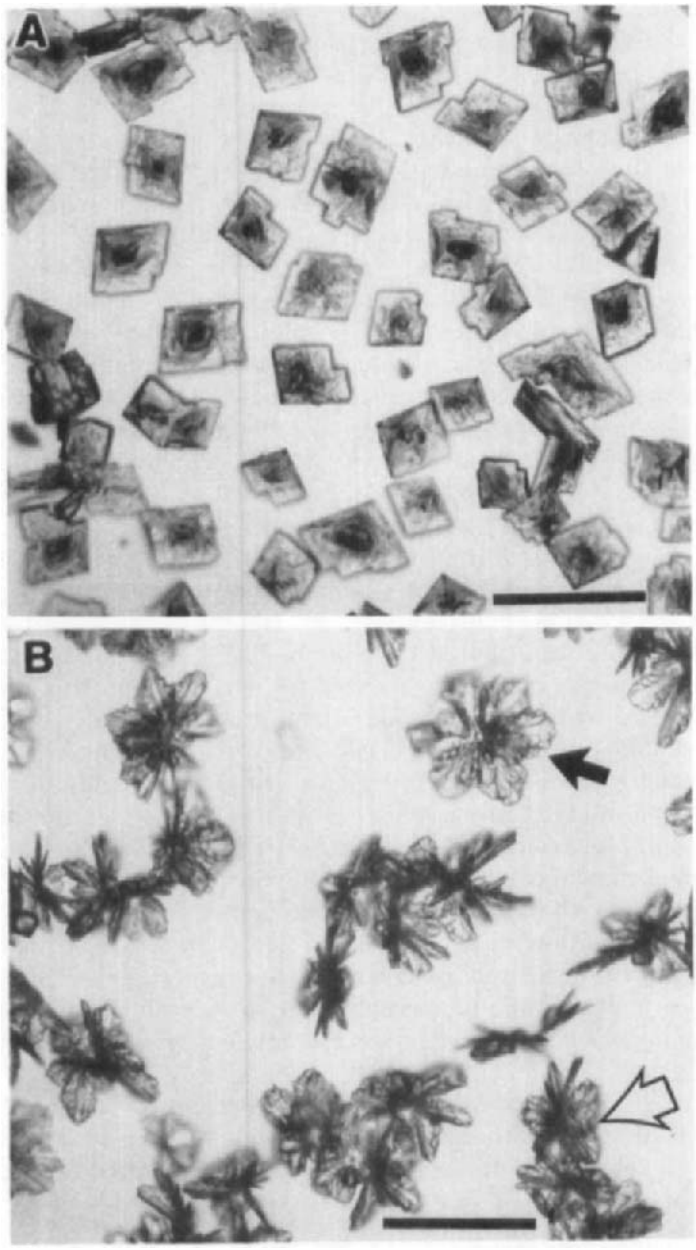

FIG. 27. Optical micrographs of (A) oriented calcite nucleated under stearate monolayers at [Ca] = 10 m*M*; bar = 100 μm. (B) Oriented vaterite crystals nucleated under octadecylamine monolayers. Arrows indicate crystals of different crystallographic orientation; bar = 100 μm.

plementarity at the inorganic/organic interface. Monolayers of simple fatty acids form hexagonal or pseudohexagonal nets of interheadgroup spacing, ~5 Å, when compressed on aqueous subphases. Thus the first layer of the crystal will be determined primarily by the two-dimensional spacings of the carboxylate-binding sites. A comparison of these distances with those between coplanar Ca atoms in the $(1\bar{1}0)$ face of calcite reveals a very close epitaxial match in two dimensions, but there is no such match for the (001) face of vaterite.

Geometric correspondence cannot, however, be solely responsible for $(1\bar{1}0)$-oriented calcite nucleation. For example, the (001) face of calcite comprises a hexagonal lattice of coplanar Ca atoms of 4.96-Å periodicity and such an arrangement matches the monolayer-binding sites almost exactly. A significant difference between the $(1\bar{1}0)$ and (001) faces is the orientation of the carbonate anions; they lie perpendicular to the $(1\bar{1}0)$ surface but parallel to (001). Thus the stereochemistry of the carboxylate headgroups mimics that of the anions in the $(1\bar{1}0)$ crystal face but not in the (001) face.

The selectivity of the (001) vaterite face on stearic acid monolayers and both (001) and (110) on octadecylamine films suggests that stereochemical factors at the interface are important, as Ca binding is not a prerequisite for oriented nucleation. Both these faces contain anions that lie perpendicular to the crystal surfaces and this motif can be mimicked by carboxylate alignment on stearic acid monolayers (Fig. 28) or bidentate binding of HCO_3^- to octadecylamine headgroups. All carbonate anions in the (001) face are perpendicular to the surface, whereas in (110) only a subset of anions have this orientation. Thus, the (001) face will be favored under carboxylate films because of the stereochemical equivalence of all the headgroups. For octadecylamine monolayers, there is no direct stereochemical correspondence, and oriented nucleation must be governed by the structure of the underlying ion-containing boundary layer. In this respect, bidentate binding of HCO_3^- at the amine headgroups will be essentially orthogonal to the monolayer surface and at least two nucleation orientations are possible.

The change from calcite to vaterite nucleation on stearate films at low [Ca] suggests that the extent of Ca binding is important for polymorph selection. The nucleation of calcite is favored by the formation of a well-defined Ca–carboxylate layer that mimics the first layer of the $(1\bar{1}0)$ face of the unit cell. By contrast, the structural requirements for vaterite formation are less precise. This is consistent with vaterite being the dominant phase on amine monolayers where no Ca binding is present, and suggests that kinetic factors of charge accumulation

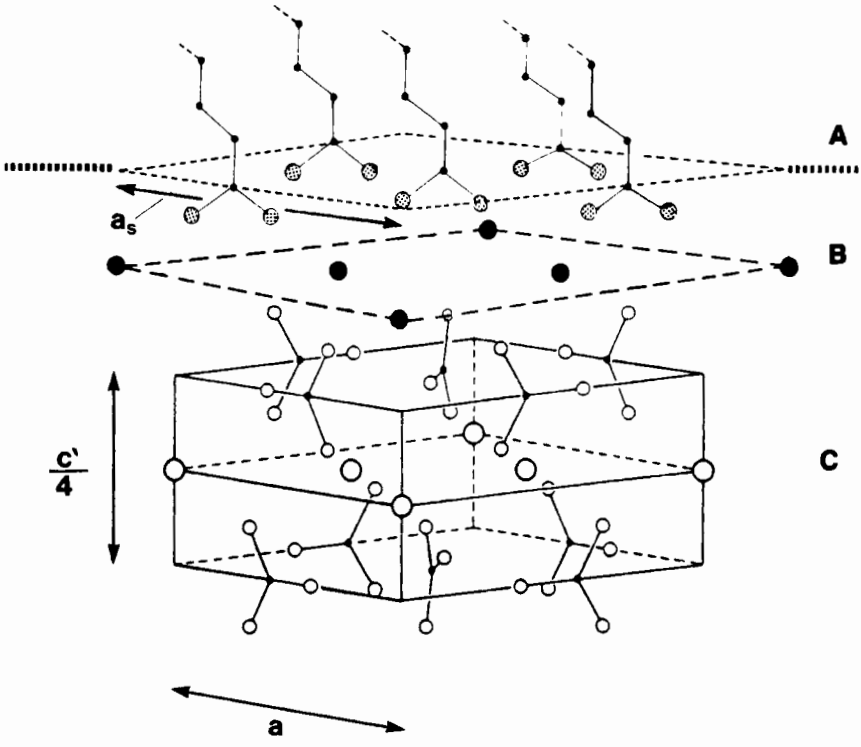

FIG. 28. Proposed organization of the interface between stearate monolayers and incipient vaterite nucleus oriented along [001]. (A) Monolayer surface showing carboxylate headgroups aligned perpendicular to the air/water interface; a_s = 8.6 Å; (B) Ca-bound layer; (C) vaterite subunit cell showing the stereochemical arrangement of carbonates perpendicular to the (001) face; c' = 17.0 Å, a = 7.15 Å. Open circles are Ca atoms in the unit cell.

and cluster stabilization overide any structural factors in these systems.

2. *Langmuir–Blodgett Films*

Crystals of $SrSO_4$ have been grown in the presence of behenic acid [$CH_3(CH_2)_{20}COOH$] Langmuir–Blodgett (LB) films (*103*). This not only allows the influence of a charged surface on crystal growth to be assessed but also the influence of an ordered hydrophobic substrate. The deposition of LB films has been developed so that carbon-coated electron microscope grids may be used as a substrate (*104*) and crystals grown on such films may be studied *in situ* at very early stages of development.

Experiments were performed under a range of supersaturation conditions with and without growth modifiers such as citrate. The highest level of control was observed at the lowest supersaturation levels investigated. Examples of crystal morphologies obtained for experiments without films and in the presence of hydrophobic and hydrophilic multilayer films are given in Fig. 29. Rhombic crystals aligned perpendicular to the [001] zone axis were observed for the control (no film) samples (Fig. 29A). The addition of trace citrate levels produced poorly formed octagonal crystals often showing evidence of secondary nucleation sites (Fig. 29B). Precipitation of $SrSO_4$ at a supersaturation 10× the solubility product in the presence of hydrophobic LB films produced disklike crystals that lay perpendicular to the [010] zone axis (Fig. 29C). Crystals deposited on hydrophilic behenic acid films at the same

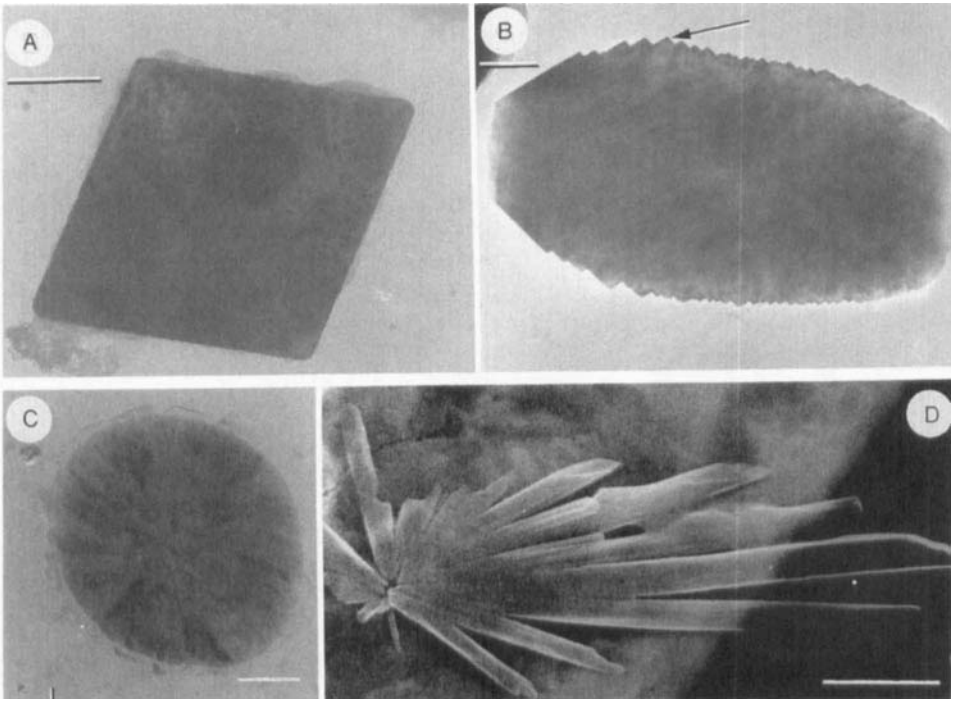

FIG. 29. EM images of synthetic strontium sulfate crystals grown from solutions at 10× solubility product. (A) Control crystals; bar = 0.5 μm. (B) In the presence of trace (10^{-6} *M*) citrate; note sites of secondary nucleation (arrow); bar = 0.2 μm. (C) Disklike crystal deposited on a hydrophobic Langmuir–Blodgett film; the crystal is aligned perpendicular to the [010] zone axis; bar = 0.2 μm. (D) Floretlike crystal deposited on a hydrophilic Langmuir–Blodgett film; bar = 1 μm.

supersaturation had a floret morphology comprising needlelike crystals growing away from the film surface (Fig. 29D). The tips of the crystallites extending from the film surface were highly beam sensitive. Electron diffraction of either the floret core or needlelike crystallites did not yield easily recognizable celestite ($SrSO_4$) diffraction patterns. It is presently thought that the underlying substrate causes distortion of the crystal lattice, and further work to identify the crystal faces expressed is in progress.

In general, the above experiments show that small perturbations in an inorganic system may directly affect crystal morphology and crystallography. Clearly these studies may have considerable biological importance, because in any compartmentalized cellular system it is possible to regulate the local supersaturation, the levels of extraneous ions, and the structure of nearby organic interfaces. Small variations only are required to induce fundamental changes in crystal nucleation and growth.

ACKNOWLEDGMENTS

We acknowledge N. P. Hughes, B. J. Liberty, C. Mortimer, E. J. Moss, S. B. Parker, T. G. Quin, A. J. Skarnulis, P. J. Strong, J. Webb, and J. R. Wilcock for their contribution to studies in biomineralization at the University of Oxford, 1977–1989. We thank J. M. Didymus, B. R. Heywood, S. Rajam, N. H. C. Sparks, V. J. Wade, and J. B. A. Walker at the University of Bath, and G. Demian, M. A. Fraser, M. W. A. Jones, S. Jordan, Y. Lin, N. Williams, and G. Yaghioglu at the University of Brunel for their involvement in this field of chemistry.

REFERENCES

1. Mann, S., Webb, J., and Williams, R. J. P., eds., "Biomineralization: Chemical and Biochemical Perspectives." VCH Pub., Weinheim, 1989.
2. Skarnulis, A. J., Strong, P. J., and Williams, R. J. P., *J. Chem. Soc., Chem. Commun.* 1030 (1978).
3. Kamatani, A., *Mar. Biol. (Berlin)* **8,** 89 (1971).
4. Mann, S., Perry, C. C., Williams, R. J. P., Fyfe, C. A., Gobbi, G. C., and Kennedy, G. J., *J. Chem. Soc., Chem. Commun.* 168 (1983).
5. Leadbeater, B. S. C., *Br. Phycol.* **7,** 195 (1972).
6. Leadbeater, B. S. C., *Protoplasma* **98,** 311 (1979).
7. Mann, S., and Williams, R. J. P., *Proc. R. Soc. London, Ser. B* **216,** 137 (1982).
8. Leadbeater, B. S. C., *Philos. Trans. R. Soc. London, Ser. B* **304,** 529 (1984).
9. Mann, S., Ph.D. Thesis, Oxford University (1982).
10. Iler, R. H., *in* "Biochemistry of Silicon and Related Problems" (G. Bendz and I. Lundqvist, eds.), pp. 53–76. Plenum, New York, 1977.

11. O'Neill, C. H., Pan Qiong-Qing, Clarke, C., Liu Fu-Sheng, Hodges, G., Ge Ming, Jordan, P., Chang Yu-Ming, Newman, R. H., and Toulson, E., *Lancet* **1,** 1202 (1982).
12. Bhatt, T., Coombes, M., and O'Neill, C. H., *Int. J. Cancer* **34,** 519 (1984).
13. Mann, S., and Perry, C. C., *Ciba Found. Symp.* **121,** 40 (1986).
14. Perry, C. C., Fraser, M. A., and Hughes, N. P., *in* "Surface Reactive Peptides and Polymers" (C. S. Sikes and A. P. Wheeler, eds.) (in press).
15. Perry, C. C., Mann, S., and Williams, R. J. P., *Proc. R. Soc. London, Ser. B* **222,** 427 (1984).
16. Perry, C. C., Moss, E. J., and Williams, R. J. P., *Proc. R. Soc. London, Ser. B* **241,** 47 (1990).
17. Perry, C. C., Williams, R. J. P., and Fry, S. C., *J. Plant. Physiol.* **126,** 437 (1987).
18. Hughes, N. P., Perry, C. C., Williams, R. J. P., Watt, F., and Grime, G. W., *Nucl. Instrum. Methods Phys. Res., Ser. B* **30,** 383 (1988).
19. Perry, C. C., and Fraser, M. A., *J. Plant Physiol.* (submitted for publication).
20. Iler, R. K., "The Chemistry of Silica." Wiley, New York, 1979.
21. Perry, C. C., Mann, S., Williams, R. J. P., Watt, F., Grime, G. W., and Takacs, J., *Proc. R. Soc. London, Ser. B* **222,** 438 (1984).
22. Grime, G. W., Watt, F., Mann, S., Perry, C. C., Webb, J., and Williams, R. J. P., *Trends Biochem. Sci.* **10,** 6 (1985).
23. Hodson, M. J., Sangster, A. G., and Parry, D. W., *Proc. R. Soc. London* **222,** 413 (1984).
24. Perry, C. C., *in* "Biomineralization" (S. Mann, J. Webb, and R. J. P. Williams, eds.), pp. 223–256. VCH Publ., Weinheim, 1989.
25. Blakemore, R. P., *Science* **190,** 377 (1975).
26. Blakemore, R. P., and Frankel, R. B., *Sci. Am.,* December, p. 42 (1981).
27. Kirschvink, J. L., *J. Exp. Biol.* **86,** 345 (1980).
28. Balkwill, D. L., Maratea, D., and Blakemore, R. P., *J. Bacteriol.* **141,** 1399 (1980).
29. Towe, K. M., and Moench, T. T., *Earth Planet. Sci. Lett.* **52,** 213 (1981).
30. Frankel, R. B., Blakemore, R. P., and Wolfe, R. S., *Science* **203,** 1355 (1979).
31. Mann, S., Moench, T. T., and Williams, R. J. P., *Proc. R. Soc. London, Ser. B.* **221,** 385 (1984).
32. Sparks, N. H. C., Mann, S., Bazylinski, D. A., Lovley, D. R., Janasch, H. W., and Frankel, R. B., *Earth Planet. Sci. Lett.* **98,** 14 (1990).
33. Mann, S., Frankel, R. B., and Blakemore, R. P., *Nature (London)* **310,** 405 (1984).
34. Torres de Arujo, F. F., Pires, M. A., Frankel, R. B., and Bicudo, C. E. M., *Biophys. J.* **50,** 375 (1985).
35. Frankel, R. B., Papaefthymiou, G. C., Blakemore, R. P., and O'Brien, W. D., *Biochim. Biophys. Acta* **753,** 147 (1983).
36. Bazylinski, D. A., Frankel, R. B., and Jannasch, H. W., *Nature (London)* **334,** 518 (1988).
37. Matsuda, T., Endo, J., Osakabe, N., and Tonamura, A., *Nature (London)* **302,** 411 (1983).
38. Mann, S., Sparks, N. H. C., and Blakemore, R. P., *Proc. R. Soc. London, Ser. B* **231,** 447 (1987).
39. Sparks, N. H. C., Courteaux, L., Mann, S., and Board, R. G., *FEMS Microbiol. Lett.* **22,** 171 (1986).
40. Mann, S., Sparks, N. H. C., and Blakemore, R. P., *Proc. R. Soc. London, Ser. B* **231,** 469 (1987).
41. Paoletti, L. C., and Blakemore, R. P., *J. Bacteriol.* **170,** 834 (1988).

42. Gorby, Y. A., Beveridge, T. J., and Blakemore, R. P., *J. Bacteriol.* **170,** 834 (1988).
43. Garrels, R. M., and Christ, C. L., "Solution, Minerals and Equilibria." Harper & Row, New York, 1965.
44. Tamura, Y., Ito, K., and Katsura, T. J., *J. Chem. Soc., Dalton Trans.* 189 (1983).
45. Harrison, P. M., Artymiuk, P. J., Ford, G. C., Lawson, D. M., Smith, J. M. A., Treffry, A., and White, J. L., *in* "Biomineralization" (S. Mann, J. Webb, and R. J. P. Williams, eds.), pp. 257–294. VCH Publ., Weinheim, 1989.
46. Treffry, A., Harrison, P. M., Cleton, M. I., de Bruijn, W. C., and Mann, S., *J. Inorg. Biochem.* **31,** 1 (1987).
47. Harrison, P. M., Fischback, F. A., Hoy, T. G., and Haggis, G. H., *Nature (London)* **216,** 1188 (1967).
48. Towe, K. M., and Bradley, W. P., *J. Colloid Interface Sci.* **24,** 384 (1967).
49. Massover, W. H., and Cowley, J. M., *Proc. Natl. Acad. Sci. U.S.A.* **70,** 3847 (1973).
50. Mann, S., Bannister, J. V., and Williams, R. J. P., *J. Mol. Biol.* **188,** 225 (1986).
51. St. Pierre, T. G., Bell, S. H., Dickson, D. P. E., Mann, S., Webb, J., Moore, G. R., and Williams, R. J. P., *Biochim. Biophys. Acta* **870,** 127 (1986).
52. Mann, S., Williams, J. M., Treffry, A., and Harrison, P. M., *J. Mol. Biol.* **198,** 405 (1987).
53. Dunkelberger, D. G., Dean, J. M., and Watabe, N., *J. Morphol.* **163,** 367 (1980).
54. Carstrom, D., *Biol. Bull. (Woods Hole, Mass.)* **125,** 441 (1963).
55. Mann, S., Parker, S. B., Ross, M. D., Skarnulis, A. J., and Williams, R. J. P., *Proc. R. Soc. London, Ser. B* **218,** 415 (1983).
56. Salamat, M. S., Ross, M. D., and Peacor, D. R., *Ann. Otol., Rhinol., Laryngol.* **89,** 229 (1980).
57. Watabe, N., *Calcif. Tissue Res.* **1,** 114 (1967).
58. Parker, S. B., Skarnulis, A. J., Westbroek, P., and Williams, R. J. P., *Proc. R. Soc. London, Ser. B* **219,** 111 (1983).
59. Mann, S., and Sparks, N. H. C., *Proc. R. Soc. London, Ser. B* **234,** 441 (1988).
60. Perry, C. C., and Wilcock, J. R., *in* "Chemical Aspects of the Regulation of Biomineralization" (C. S. Sikes and A. P. Wheeler, eds.), p. 39. University of Alabama Publication Services, 1989.
61. Wilcock, J. R., Perry, C. C., and Williams, R. J. P., *Proc. R. Soc. London, Ser. B* **233,** 393 (1988).
62. Hughes, N. P., Perry, C. C., Anderson, O. R., and Williams, R. J. P., *Proc. R. Soc. London, Ser. B* **238,** 223 (1989).
63. Anderson, O. R., Perry, C. C., and Hughes, N. P., *Phil. Trans. R. Soc. London, Ser. B* **329,** 81 (1990).
64. Wilcock, J. R., Perry, C. C., and Williams, R. J. P., *Proc. R. Soc. London, Ser. B* **238,** 203 (1989).
65. Perry, C. C., Wilcock, J. R., Brook, A. R., and Williams, R. J. P., *Proc. R. Soc. London, Ser. B* (submitted for publication).
66. Wilbur, K. M., and Watabe, N., *Ann. N.Y. Acad. Sci.* **109,** 82 (1963).
67. Klaveness, D., *Protistologica* **8,** 335 (1972).
68. van der Wal, P., de Jong, E. W., Westbroek, P., and de Bruijn, W. C., *Protoplasma* **118,** 157 (1983).
69. Fitchinger-Schepmann, A. M. J., Ph.D. Thesis, University of Utrecht (1980).
70. Borman, A. H., de Jong, E. W., Huizinga, M., Kok, D. J., Westbroek, P., and Bosch, L., *Eur. J. Biochem.* **129,** 179 (1982).
71. Schewiakoff, W., *Fauna Flora Golfes Neapel* 37 (1926).
72. Perry, C. C., Wilcock, J. R., and Williams, R. J. P., *Experientia* **44,** 638 (1987).

73. Picket-Heaps, J. D., *Mod. Cell Biol.* **2,** 241 (1983).
74. Lowenstam, H. A., *Science* **137,** 279 (1962).
75. Sollas, I. B. J., *Q. J. Microsc. Sci.* **51,** 115 (1907).
76. Runham, N. W., Thornton, P. R., Shaw, D. A., and Wayte, R. C., *Z. Zellforsch. Mikrosk. Anat.* **99,** 608 (1969).
77. Grime, G. W., Watt, F., Mann, S., Perry, C. C., Webb, J., and Williams, R. J. P., *Trends Biochem. Sci.* **10,** 6 (1985).
78. Webb, J., St. Pierre, T. G., Dickson, D. P. E., Mann, S., Williams, R. J. P., Perry, C. C., Grime, G. W., Watt, F., and Runham, N. W., *in* "Frontiers of Bioinorganic Chemistry" (A. V. Xavier, ed.), pp. 441–452. VCH Publ., Weinheim, 1986.
79. Runham, N. W., *Q. J. Microsc. Sci.* **102,** 371 (1961).
80. Mann, S., Perry, C. C., Webb, J., Luke, B., and Williams, R. J. P., *Proc. R. Soc. London, Ser. B* **227,** 179 (1986).
81. St. Pierre, T. G., Mann, S., Webb, J., Dickson, D. P. E., Runham, N. W., and Williams, R. J. P., *Proc. R. Soc. London, Ser. B* **228,** 31 (1986).
82. Hutchison, J. L., Mann, S., Skarnulis, A. J., and Williams, R. J. P., *J. Chem. Soc., Chem. Commun.* 634 (1980).
83. Mann, S., and Williams, R. J. P., *J. Chem. Soc., Dalton Trans.* 311 (1983).
84. Mann, S., Skarnulis, A. J., and Williams, R. J. P., *Isr. J. Chem.* **21,** 3 (1981).
85. Heywood, B. R., and Eanes, E. D., *Calcif. Tissue Int.* 41, 192 (1987).
86. Mann, S., Hannington, J. P., and Williams, R. J. P., *Nature (London)* **324,** 565 (1986).
87. Mann, S., and Hannington, J. P., *J. Colloid Interface Sci.* **122,** 326 (1988).
88. Bhandarkar, S., and Bose, A., *J. Colloid Interface Sci.* **135,** 531 (1990).
89. Perry, C. C., *in* "Proceedings of the 1st A.N.A.I.C. Conference on Si and Sn." Oxford Univ. Press, Oxford (in press).
90. Parker, S. B., Ph.D. Thesis, Oxford University (1984).
91. Mann, S., Kime, M. J., Ratcliffe, R. G., and Williams, R. J. P., *J. Chem. Soc., Dalton Trans.* 771 (1983).
92. Wheeler, A. P., George, J. W., and Evans, C. A., *Science* **212,** 1397 (1981).
93. Berman, A., Addadi, L., and Weiner, S., *Nature (London)* **331,** 546 (1988).
94. Mann, S., Didymus, J. M., Sanderson, N. P., and Heywood, B. R., *J. Chem. Soc., Faraday Trans.* **86,** 1873 (1990).
95. Ross, M. D., and Pote, K. G., *Philos. Trans. R. Soc. London, Ser. B* **304,** 445 (1984).
96. Weiner, S., and Traub, W., *Philos. Trans. R. Soc. London, Ser. B* **304,** 425 (1984).
97. Addadi, L., and Weiner, S., *Proc. Natl. Acad. Sci. U.S.A.* **82,** 4110 (1985).
98. Landau, E. M., Popovitz-Bior R., Levanon, M., Leiserowitz, L., Lahav, M., and Sagiv, J., *Mol. Cryst. Liq. Cryst.* **134,** 323 (1986).
99. Landau, E. M., Grayer Wolf, S., Levanon, M., Leiserowitz, L., Lahav, M., and Sagiv, J., *J. Am. Chem. Soc.* **111,** 1436 (1989).
100. Mann, S., Heywood, B. R., Rajam S., and Birchall, J. D., *Nature (London)* **334,** 692 (1988).
101. Mann, S., Heywood, B. R., Rajam S., and Birchall, J. D., *Proc. R. Soc. London, Ser. A* **423,** 457 (1989).
102. Mann, S., Heywood, B. R., Rajam S., Walker, J. B. A., Davey, R. J., and Birchall, J. D., *Adv. Mater.* **2,** 257 (1990).
103. Hughes, N. P., Heard, D., Perry, C. C., and Williams, R. J. P., *J. Appl. Phys.* (in press).
104. Heard, D., Roberts, G. G., Holcroft, B., and Goringe, M. J., *Thin Solid Films* **160,** 491 (1988).